

1 **Journal: ACP - MS No.: acp-2020-84**

2 **Title: Molecular Insights into New Particle Formation in Barcelona, Spain**

3 **Author(s): Brean et al.**

4

5

RESPONSE TO THE EDITOR

6

7 Referee comments in this text will appear in blue, responses in black, and where new text from the
8 manuscript is quoted, it will appear in red, and **bold** where text has been inserted into a larger section

9

10 *Comment 1: Referring to the first comment by referee 1, the multiplication factor in calculating CS should indeed be*
11 *2πD, not 4πD as in equation 1 or incorrectly given in Kulmala et al. 2012. Note that in the original paper by Kulmala et*
12 *al. 2001 which introduced CS, there is 4πD but that is multiplied by the particle radius, not diameter as currently in*
13 *practice. Unfortunately, this has caused plenty of confusion during recent years. I would encourage the authors to correct*
14 *this point: at the end it has little influence on the actual results, affecting mainly the absolute values of reported CS.*

15 **Response 1:** This has been amended in the methods section, further, we have fixed these values both in our figures
16 (Figures 3, and S2) and in the text (line 280)

17

18 *Comment 2: In general, the paper is very clearly written and with a proper language. However, the following should be*
19 *checked out:*

- 20 1) in many places it reads "between M-N" although it should be either "between M and N" or "in the range of M-N",
- 21 2) in some of the new text, articles seems to be missing,
- 22 3) the text in section 2.4 requires some improvements, please check out.

23 **Response 2:**

24 1) These have been fixed through the text and supplement

25 2) These have been added throughout the text, alongside an error in one of the references in-line

26 3) We have amended the final paragraph of this section to now read

27 *"...where N_C , N_H , and N_N , are the number of carbon, hydrogen, and nitrogen atoms respectively.*
28 *N_O is the number of oxygen atoms minus $3N_N$ to account for $-ONO_2$ groups, N_{C0} is 25 (the carbon*
29 *number of an alkane with a saturation mass concentration of $1 \mu\text{g m}^{-3}$), b_C , b_O , b_{CO} , and b_N are*
30 *0.475, 0.2, 0.9 and 2.5 respectively, and represent interaction and nonideality terms. The final term*
31 *of equation (4) account for $-ONO_2$ groups, each reducing the saturation vapour pressure by 2.5*
32 *orders of magnitude. C^* values are calculated at 300 K and not corrected for temperature, as 300 K*
33 *is within 1 K of the campaign average temperature."*

34

35 *Comment 3: The term "high ozone" does sound scientifically correct, should it rather be "high ozone concentration"?*

36 **Response 3:** This has been added to the relevant lines (264 & 480)

37

38 *Comment 4: On lines 391-392 in the file marked by track changes, should one write "...with an increasing temperature"?*

39

40 **Response 4:** This has been changed and now reads as follows

41 *"Model studies of sulphuric acid-amine nucleation show a decline in nucleation rate with an*
42 *increasing temperature"*

43

44 *Comment 5: The information in Yan et al (2018) in the reference list seems to be incomplete. Please correct.*

45 **Response 5:** This has been amended. Alongside this, we tidy up minor errors in some other references.

46

47
48
49
50
51
52
53
54
55
56
57
58
59
60
61
62
63
64
65
66
67
68
69
70
71
72

Molecular Insights into New Particle Formation in Barcelona, Spain

**James Brean¹, David C.S. Beddows¹, Zongbo Shi¹,
Brice Temime-Roussel², Nicolas Marchand², Xavier Querol³,
Andrés Alastuey³, María Cruz Minguillón³, and
Roy M. Harrison^{1a*}**

**¹Division of Environmental Health and Risk Management
School of Geography, Earth and Environmental Sciences
University of Birmingham, Edgbaston, Birmingham B15 2TT
United Kingdom**

**²Aix Marseille Univ, CNRS, LCE
Marseille, 13003, France**

**³Institute of Environmental Assessment and
Water Research (IDAEA-CSIC), Barcelona, 08034 Spain**

**^aAlso at: Department of Environmental Sciences / Center of
Excellence in Environmental Studies, King Abdulaziz University, PO
Box 80203, Jeddah, 21589, Saudi Arabia**

* To whom correspondence should be addressed (Email: r.m.harrison@bham.ac.uk)

73 **ABSTRACT**

74 Atmospheric aerosols contribute some of the greatest uncertainties to estimates of global radiative
75 forcing, and have significant effects on human health. New particle formation (NPF) is the process
76 by which new aerosols of sub-2 nm diameter form from gas-phase precursors and contributes
77 significantly to particle numbers in the atmosphere, accounting for approximately 50% of cloud
78 condensation nuclei globally. Here, we study summertime NPF in urban Barcelona in NE Spain
79 utilising particle counting instruments down to 1.9 nm and a Nitrate CI-API-ToF. The rate of
80 formation of new particles is seen to increase linearly with sulphuric acid concentration, although
81 particle formation rates fall short of chamber studies of H₂SO₄-DMA-H₂O, while exceeding those
82 of H₂SO₄-BioOxOrg-H₂O nucleation, although a role of highly oxygenated molecules (HOMs)
83 cannot be ruled out. The sulphuric acid dimer:monomer ratio is significantly lower than that seen in
84 experiments involving sulphuric acid and DMA in chambers, indicating that stabilization of
85 sulphuric acid clusters by bases is weaker in this dataset than in chambers, either due to rapid
86 evaporation due to high summertime temperatures, or limited pools of stabilising amines. Such a
87 mechanism cannot be verified in this data, as no higher-order H₂SO₄-amine clusters, nor H₂SO₄-
88 HOM clusters were measured. The high concentrations of HOMs arise from isoprene, alkylbenzene,
89 monoterpene and PAH oxidation, with alkylbenzenes providing greater concentrations of HOMs
90 due to significant local sources. The concentration of these HOMs shows a dependence on
91 temperature. The organic compounds measured primarily fall into the SVOC volatility class arising
92 from alkylbenzene and isoprene oxidation. LVOC largely arise from oxidation of alkylbenzenes,
93 PAHs and monoterpenes, whereas ELVOC arise from primarily PAH and monoterpene oxidation.
94 New particle formation without growth past 10 nm is also observed, and on these days oxygenated
95 organic concentrations are lower than on days with growth by a factor of 1.6, and thus high
96 concentrations of low volatility oxygenated organics which primarily derive from traffic-emitted
97 VOCs appear to be a necessary condition for the growth of newly formed particles in Barcelona.
98 These results are consistent with prior observations of new particle formation from sulphuric acid-

99 amine reactions in both chambers and the real atmosphere, and are likely representative of the urban
100 background of many European Mediterranean cities. A role for HOMs in the nucleation process
101 cannot be confirmed or ruled out, and there is strong circumstantial evidence for the participation of
102 HOMs across multiple volatility classes in particle growth.

103

104

105 1. INTRODUCTION

106 Atmospheric aerosols, defined as liquid or solid droplets suspended in a gas, affect the climate both
107 directly by scattering and absorbing radiation, and indirectly by acting as cloud condensation nuclei
108 (CCN) (Penner et al., 2011), providing great uncertainties in estimates of global radiative forcing
109 (IPCC, 2014). Further, fine ambient aerosols (defined as those with diameter below 2.5 μm) are the
110 fifth greatest global mortality risk factor, resulting in 103.1 million disability-adjusted life year loss
111 in 2015 (Cohen et al., 2017). The number concentration of the ultrafine fraction of these (aerosols
112 with diameter below 0.1 μm , referred to as ultrafine particles or UFP) pose potentially significant
113 health risks also, due to their high concentration and surface area. The more diffuse, gas-like
114 behaviour of UFP allows them to penetrate into the deep lung and enter the bloodstream (Miller et
115 al., 2017). Ultrafine particles occur in the urban environment either as primary emissions (e.g., from
116 car exhaust (Harrison et al., 2018)) or secondarily as the product of new particle formation (NPF)
117 (Brines et al., 2015; Guo et al., 2014; Kulmala et al., 2017; Lee et al., 2019)

118

119 NPF is the formation of aerosol particles from gas-phase precursors. NPF can be considered a two-
120 step process involving initial formation of a cluster of gas molecules at the critical diameter at
121 around 1.5 nm - the diameter at which a free-energy barrier must be overcome to allow the
122 spontaneous phase transition from gas to liquid or solid (Zhang et al., 2012), and the subsequent
123 growth of this droplet to a larger aerosol particle. The first step of this process is dependent upon
124 the stability and abundance of the clustering molecules. Sulphuric acid, water, and dimethylamine
125 (DMA), for example, efficiently form particles as the strong hydrogen bonding between the acid
126 base pair produces near negligible evaporation, much lower than the evaporation rate seen for the
127 more weakly bound sulphuric acid-ammonia-water system. Nucleation of sulphuric acid, DMA and
128 water proceeds at, or near to the kinetic limit in a chamber at 278 K when DMA mixing ratios are
129 sufficient (Almeida et al., 2013; Kürten et al., 2014). Once past this 1.5 nm diameter, condensation
130 and coagulation will drive particle growth. Both the abundance of condensable gases and their

131 vapour pressures limit condensational growth. Vapour pressures are especially important for the
132 initial growth stages, as the Kelvin effect barrier impairs condensation of more volatile species, with
133 this condition of low vapour pressures becoming less significant as the diameter of the particle
134 increases (Tröstl et al., 2016). Once sufficiently large (>50 nm), the loss processes of coagulation
135 and evaporation of these particles become inefficient, resulting in a significant atmospheric lifetime.
136 It is from these these diameters onwards the climate forcing effects of these particles become most
137 pronounced.

138

139 NPF processes happen globally, across a diverse range of environments from pristine polar regions,
140 to polluted urban megacities (Kerminen et al., 2018), and represent a significant source of CCN,
141 with 10-60% of NPF events shown to produce CCN and enhancement factors to CCN count ranging
142 from 0.5 – 11 (Lee et al., 2019 and references within). Strong NPF events are observed across a
143 range of urban environments, despite high condensation sinks $>10^{-2} \text{ s}^{-1}$ (Bousiotis et al., 2019; Yu et
144 al., 2016), and can act as a precursor to strong haze events (Guo et al., 2014). The occurrence of
145 urban NPF has only been partially explained by growing understanding from recent in-depth studies
146 (Yao et al., 2018). Recent advances in instrumentation allow for the measurement of particles down
147 to the critical diameter with instruments such as the particle size magnifier (PSM), and (Neutral) Air
148 Ion Spectrometer (NAIS/AIS) (Lee et al., 2019), and mass spectral techniques for measuring the
149 abundance and composition of neutral (Jokinen et al., 2012) and charged (Junninen et al., 2010)
150 clusters. Elucidated mechanisms with these techniques involve sulphuric acid and ammonia in
151 remote environments (Jokinen et al., 2018; Yan, 2018), monoterpene derived highly oxygenated
152 molecules (HOM) in remote environments (Rose et al., 2018), iodic acid in coastal environments
153 (Sipilä et al., 2016), and sulphuric acid and DMA in polluted urban environments (Yao et al., 2018).

154

155 Urban Barcelona sees frequent, strong summer-time NPF events occurring on 28% of days. These
156 events are associated with high insolation and elevated ozone ($\sim 60 \mu\text{g m}^{-3}$) when considering the

157 whole year (Brines et al., 2014, 2015). Ground-level observations report NPF events starting
158 typically at midday, and either occurring in urban Barcelona and the surrounding regional
159 background simultaneously, or isolated to either urban Barcelona or just the regional background
160 (Dall'Osto et al., 2013). Vertical profiles over urban Barcelona reveal that NPF occurs at higher
161 altitudes, and starts earlier in the day, as at a given altitude these events are not suppressed by early
162 traffic peaks contributing to particle load (Minguillón et al., 2015). Here, we examine gas phase
163 mass spectral evidence and particle formation rates at the critical diameter from sulphuric acid in
164 Barcelona, with possible contribution from strong bases and highly oxygenated organic molecules
165 (HOMs), as well as factors influencing subsequent particle growth.

166

167 **2. METHODS**

168 **2.1 Sampling Site**

169 The Palau Reial site in Barcelona (41°23'15" N, 2°6'53.64" E) is representative of the urban
170 background of Barcelona, located at the Institute of Environmental Assessment and Water Research
171 (IDAEA-CSIC) in the north-west of the city. Sampling was performed from a container 20 m from
172 a low traffic road, and 200 m from the nearest main road (Avinguda Diagonal). Data were taken
173 from 2018/06/28 through 2018/07/18.

174

175 **2.2 Chemical Ionisation Atmospheric Pressure Interface Time of Flight Mass**

176 **Spectrometry**

177 The Aerodyne Nitrate Chemical Ionisation Atmospheric Pressure interface Time of Flight Mass
178 Spectrometer (CI-APi-ToF) was used to make measurements of neutral oxygenated organic
179 compounds, organic and inorganic acids, bases, and their molecular clusters at high time resolution
180 with high resolving power. The ionization system charges molecules by adduct formation, such as
181 in the case of organic compounds with two or more hydrogen bond donor groups (Hytinen et al.,
182 2015), or proton transfer in the case of strong acids like sulphuric acid (Jokinen et al., 2012).

183 Hydroxyl or hydroperoxyl functionalities are both common hydrogen bond donating groups, with
184 hydroperoxyl being the more efficient hydrogen bond donor (Møller et al., 2017). This instrument
185 has been explained in great detail elsewhere (Jokinen et al., 2012; Junninen et al., 2010), but briefly,
186 the front end consists of a chemical ionisation system where a 10 L min^{-1} sample flow is drawn in
187 through the 1 m length 1" OD stainless steel tubing opening. A secondary flow was run parallel and
188 concentric to this sample flow, rendering the reaction chamber effectively wall-less. A $3 \text{ cm}^3 \text{ min}^{-1}$
189 flow of a carrier gas (N_2) is passed over a reservoir of liquid HNO_3 , entraining vapour which is
190 subsequently ionised to NO_3^- via an X-ray source. Ions are then guided into the sample flow. The
191 nitrate ions will then charge molecules either by clustering or proton transfer. The mixed flows
192 travelling at 10 L min^{-1} enter the critical orifice at the front end of the instrument at 0.8 L min^{-1} and
193 are guided through a series of differentially pumped chambers before reaching the ToF analyser. All
194 data analysis was carried out in the Tofware package in Igor Pro 7 (Tofwerk AG, Switzerland).
195 Signals except for those of amines and ammonia are divided by the sum of reagent ion signals and
196 multiplied by a calibration coefficient to produce a concentration. A calibration coefficient of 3×10^9
197 cm^{-3} was established based upon comparison with a sulphuric acid proxy (Mikkonen et al., 2011)
198 and is in line with a prior calibration with our instrument (Brean et al., [2019](#)[2020](#)). Uniform
199 sensitivity between H_2SO_4 and all other species measured by CI-APi-ToF bar amines and ammonia
200 was assumed in this work. This introduces some uncertainties, as it relies upon both collision rates
201 and charging efficiencies to be the same within the ionisation source for all species. Amine and
202 ammonia signals are normalised to the nitrate trimer signal (Simon et al., 2016). Prior reports of
203 ammonia and amines as measured by CI-APi-ToF employed corona discharge systems, which
204 utilise higher concentrations of nitric acid, thus we report normalised signals. We present
205 correlations of each of these bases clustered with the nitrate dimer plotted against measurements
206 with the nitrate trimer, as well as their intercorrelations and example peak fits across Figure S1. C_2
207 amines, C_4 amines and ammonia were the only molecules of this kind found in our mass spectra.
208 Systematic uncertainties of +100% / -50 % arising from this method are assumed.

209 Due to the high resolving power of the CI-APi-ToF system (mass resolving power of 3000, and
210 mass accuracy of 20 ppm at 201 m/Q), multiple peaks can be fit at the same unit mass and their
211 molecular formulae assigned. Beyond 500 m/Q, peak fitting and assignment of compositions
212 becomes problematic as signal decreases, mass accuracy decreases, and the total number of possible
213 chemical compositions increases, so peaks above the C₂₀ region have not been assigned (Cubison
214 and Jimenez, 2015), however, signals past this region tended to be extremely low. All ions
215 identified are listed in Table S1. As proton transfer mostly happens with acids, and nearly all HOM
216 molecules will be charged by adduct formation it is possible to infer the uncharged formula;
217 therefore, all HOMs from here onwards will be listed as their uncharged form. The CI-APi-ToF
218 inlet was placed approximately 1.5 m a.g.l. CI-APi-ToF data is only available between the dates
219 2018/07/06 and 2018/07/17.

220

221 **2.2 Particle Size and Number Measurements**

222 Two Scanning Mobility Particle Sizer (SMPS) instruments measured particle size distributions at 5
223 minute time resolution, one Long Column SMPS (TSI 3080 EC, 3082 Long DMA, 3772 CPC, TSI,
224 USA) and one NanoSMPS (3082 EC, 3082 Nano DMA, 3776 CPC, TSI, USA) measuring the
225 ranges 10.9 – 478.3 nm and 4.5 – 65.3 nm respectively. A Particle Size Magnifier (A10, Airmodus,
226 FN) linked to a CPC (3775, TSI, USA) measured the sub-3 nm size fraction. The PSM was run in
227 stepping mode, operating at four different saturator flows to vary the lower size cut of particles that
228 it will grow (defined as the point of 50% efficiency, D₅₀). The instrument provided D₅₀ from 1.4 to
229 2.4 nm. The instrument switched between saturator flows each 2.5 minutes, giving a sub-2.4 nm
230 size distribution every 10 minutes. Aerosol sampling inlets were placed approximately 2 m a.g.l.

231

232 **2.3 Other Measurements**

233 Mixing ratios of non-methane VOC with proton affinity greater than H₃O⁺ were made using the
234 proton transfer reaction time of flight mass spectrometer (PTR-ToF-MS 8000, Ionicon Analytik

235 GmbH, Austria). A detailed description of the instrument is provided by Graus et al., (2010) The
 236 sampling set up, operating conditions, and quantification procedures are similar to those described
 237 in Minguillón et al. (2016). Continual monitoring of composition and mass of submicron aerosol
 238 >75 nm was carried out with an Aerosol Chemical Speciation Monitor (ACSM, Aerodyne, USA)
 239 (Ng et al., 2011). Ozone, NO, and NO₂ were measured by conventional ultraviolet and
 240 chemiluminescence air quality instrumentation. Meteorological data were supplied by the Faculty of
 241 Physics of University of Barcelona, from a nearby (200 m from the measurement site)
 242 meteorological station located at the roof of an 8 floor building.

243

244 **2.4 Condensation Sink and Particle Growth Rate**

245 The condensation sink (CS) represents the rate at which a vapour phase molecule will collide with
 246 pre-existing particle surface, and was calculated from the size distribution data as follows (Kulmala
 247 et al., 2012):

248

$$249 \quad CS = 24\pi D \sum_{d_p} \beta_{m,d_p} d_p N_{d_p}, \quad (1)$$

250

251 where D is the diffusion coefficient of the diffusing vapour (assumed sulphuric acid), β_m is a
 252 transition regime correction (Kulmala et al., 2001), d_p is particle diameter, and N_{d_p} is the number of
 253 particles at diameter d_p . The formation rate of new particles at size d_p is calculated as follows:

254

$$255 \quad J_{d_p} = \frac{dN_{d_p}}{dt} + CoagS_{d_p} \cdot N_{d_p} + \frac{GR}{\Delta d_p} \cdot N_{d_p} \quad (2)$$

256

257 where the first term on the right-hand side comprises the rate at which particles enter the size d_p ,
 258 and the latter two terms represent losses from this size by coagulation and growth respectively. J_5

259 was calculated using the data between-in the range of 5 – 10 nm, and $J_{1.9}$ was calculated using the
 260 measurements between-in the range of 1.9 – 4.5 nm. We also calculated $J_{1.9}$ from our NanoSMPS

261 data, employing the equations of Lehtinen et al. (2007). $J_{1.9}$ from both methods showed reasonable
262 agreement ($R^2 = 0.34$). Agreement between J_5 and $J_{1.9}$ for each method was similar ($R^2 = 0.37$ and
263 $R^2 = 0.38$ for $J_{1.9}$ calculated from PSM data and from Lehtinen et al. (2019) respectively). $J_{1.9}$ is
264 greater than J_5 as predicted from equation (2) by around a factor of 20. See Kulmala et al. (2001) for
265 more information on calculation of coagulation sinks and formation rates. Growth rates ~~between-in~~
266 ~~the range of~~ 4.5 – 20 nm were calculated according to the lognormal distribution function method
267 (Kulmala et al., 2012), whereas those ~~between-in the range of~~ 1.9 ~~– and~~ 4.5 nm were calculated
268 from PSM data using a time-delay method between PSM and NanoSMPS data. Systematic
269 uncertainties on our calculated $J_{1.9}$ values include 25% method uncertainty (Yli-Juuti et al., 2017),
270 with a further 25% arising from uncertainties in PSM cutoff (± 0.5 nm), as well as a 10%
271 uncertainty in counting errors. A 50% error arising from calculated coagulation sink is also applied
272 (~~Kürten-Kurtén~~ et al., 2016). The above calculations rely on the assumption of homogeneous air
273 masses, and while air mass advection, as well as primary particle emissions can cause errors in
274 estimations of temporal changes in particle count and diameter, the appearance and persistence of a
275 new mode of particles across a period of several hours is typically indicative of a regional process.
276
277 Growth rates from irreversible condensation of various vapours were calculated as according to
278 Nieminen et al. (2010). At our measured relative humidity, sulphuric acid favours binding to 2 H₂O
279 molecules (~~Kürten-Kurtén~~ et al., 2007). As amine concentrations are likely limited, we presume no
280 mass from amines in the condensing species. H₂SO₄ was assigned a density of 1.8 g cm⁻³. For
281 simplicity, the properties of MSA regarding density and hydration were presumed the same as
282 H₂SO₄, and HIO₃ was presumed to have the same hydration as H₂SO₄, with a density of 4.98 g cm⁻³.
283 The density of condensing organic vapours was assumed 1.5 g cm⁻³, and concentration-weighted
284 mean mass (~ 276 g mol⁻¹ for LVOC) and atomic weighted diffusion volumes of organic compounds
285 were used to calculate GRs.

286

287 2.4 DBE and 2D-VBS

288 The double bond equivalent (DBE) describes the degree of unsaturation of an organic molecule and
289 is defined simply as:

290

$$291 \text{ DBE} = N_C - \frac{N_H}{2} - \frac{N_N}{2} + 1 \quad (3)$$

292

293 The saturation vapour pressure at 300 K is defined by the 2D-volatility basis set (2D-VBS) as
294 follows, if all nitrogen functionality is assumed to take the form -ONO₂ (Bianchi 2019; Donahue
295 2011; Schervish and Donahue, 2020):

296

$$297 \text{ Log}_{10}(C^*)(300 \text{ K}) = (N_{C0} - N_C)b_C - N_O b_O - 2 \frac{N_O N_C}{N_C + N_O} b_{CO} - N_n b_N \quad (4)$$

298

299 where N_C, N_H, and N_N, are the number of carbon, hydrogen, and nitrogen atoms respectively. N_O is
300 the number of oxygen atoms minus 3N_N to account for -ONO₂ groups, N_{C0} is 25 (the carbon
301 number of an alkane with a saturation mass concentration of 1 μg m⁻³-alkane), b_C, b_O, b_{CO}, and b_N
302 are 0.475, 0.2, 0.9 and 2.5 respectively, and represent interaction and nonideality terms. The final
303 term of equation (4) represents the accounts for -ONO₂ groups, each reducing the saturation vapour
304 pressure by 2.5 orders of magnitude. C* values are calculated at 300 K and not corrected for
305 temperature, as 300 K is within 1 K of the campaign average temperature.

306

307 3. RESULTS AND DISCUSSION

308 3.1 General Conditions of NPF Events

309 Summer NPF events in the regional background around Barcelona are associated with high

310 insolation, relatively low ozone concentration (high compared with the rest of the year), and lower
311 particulate matter load (Brines et al., 2014; Carnerero et al., 2019). Figure 1 shows an example of a
312 day with no NPF in panel (a), referred to as “non-event” here, where two traffic-associated peaks in

313 particle number are seen during rush hours. Midday traffic peaks are also seen on certain days, but
314 these are easily distinguished from nucleation processes due to the lack of a significant <10 nm
315 mode. Figure 1(b) shows a nucleation day with growth to larger sizes >10 nm, termed “full-event”,
316 showing the growth through the course of the day. These fulfil all the criteria of Dal Maso et al.
317 (2005). 4 events of this type were observed with CI-API-ToF data coverage. Figure 1(c) shows a
318 day with nucleation occurring, but no growth past 10 nm. These days are referred to as “burst-
319 event” days. Here, NPF is seen to occur, but particles fail to grow past the nucleation mode. 2 such
320 events were seen in this data with CI-API-ToF data coverage, and both are accompanied by a
321 distinct mode appearing beforehand in the range of at ~20 – 40 nm. Condensation sinks were not
322 significantly higher than on full event days, so this failure of particles to grow further cannot be
323 attributed to condensational (or coagulation) losses. $GR_{4.5-20}$ ranged between 2.47 ~~–~~ and 7.31 $nm\ h^{-1}$
324 $(4.69 \pm 2.03\ nm\ h^{-1})$, $GR_{1.9-4.5}$ ranged between 3.12 ~~–~~ and 5.20 $nm\ h^{-1}$ $(4.36 \pm 1.02\ nm\ h^{-1})$. The
325 survival parameter (P) as suggested by Kulmala et al. (2017) is defined as $CS \cdot 10^{-4} / GR$, and for this
326 data is equal to 8241, higher than other European cities. ~~The occurrence of such a high P value~~
327 ~~should, in theory, inhibit the occurrence of NPF, but we show events happen readily under such~~
328 ~~conditions, akin to other heavily polluted megacities.~~

329
330 Figure 2 contains box plots showing condensation sink, temperature and global radiation for all 3
331 NPF types across the entire day (diurnal profiles plotted in Figure S2). Condensation sinks during
332 NPF periods of both types (Figures 1(b) & 1(c)) were not significantly lower than in non-event
333 periods. Condensation sinks were suppressed prior to the beginning of an event for full-events,
334 increasing relative to non-events through the afternoon period. Of the two burst-events, one was
335 similarly characterised by a suppression to condensation sink, whereas the other showed a sharp rise
336 in the midday. Global radiation and temperature were higher for full-events, most significantly for
337 temperature. Figure 3 is as Figure 2 but for sulphuric acid, ammonia and amines, and HOMs as
338 measured by CI-API-ToF (HOM criteria are discussed in section 3.3.1). Sulphuric acid is elevated

339 during both full-event and burst-event periods. In urban Barcelona, sulphuric acid will primarily
340 arise from oxidation of SO₂ by the OH· radical, with anthropogenic emissions such as shipping
341 emissions from the port areas being significant sources of SO₂ (Henschel et al., 2013). Direct traffic
342 emissions have been shown to be a significant primary sulphuric acid source (Olin et al., 2020), but
343 our sulphuric acid data show no traffic peaks. Ammonia and amines show enhancement for full-
344 event periods, but not burst-event periods. Nucleation rates (at typical tropospheric sulphuric acid
345 concentrations) are sensitive to amine concentrations in the range of a few pptv, with enhancements
346 to amine mixing ratios past this point increasing the nucleation rate marginally (Almeida et al.,
347 2013), while typical concentrations of DMA and other alkylamines vary from zero to a few pptv in
348 the boundary layer (Ge et al., 2011a).

349

350 Barcelona has been shown to contain ppbv levels of ammonia (Pandolfi et al., 2012), arising from
351 both agriculture to the north (Van Damme et al., 2018), and anthropogenic activities such as waste
352 management and traffic, with waste management being the primary ammonia source. Highest
353 ammonia mixing ratios are found in the densely populated old city centre (Reche et al., 2015).
354 Agriculture, waste management, and traffic are also all significant sources of low molecular weight
355 alkylamines, such as DMA (Ábalos et al., 1999; Cadle and Mulawa, 1980; Hutchinson et al., 1982;
356 Ge et al., 2011a), and are likely the source of amines found in this dataset. Activities such as
357 composting and food industry are especially strong sources of trimethylamine (TMA) (Ge et al.,
358 2011a). Although high emission fluxes of TMA are expected in this environment, they are not
359 present in our spectra. The TMA ion has been reported previously with a similar ionisation setup to
360 that utilised in this study (Kürten et al., 2016). On full-event days, the signal for C₂ and C₄ amines
361 has a midday elevation concurrent with peaks to solar radiation (Figure S2), and can help explain
362 the high formation rates we see in this dataset (see section 3.2). The relative strength of these
363 signals are shown in Figure S3, with significantly higher signals attributed to ammonia compared to
364 amines, despite a likely lower sensitivity (Simon et al., 2016).

365

366 HOM concentrations were greatly enhanced during full-event periods (factor of 1.5 higher
367 compared to non-NPF mean), but lower during burst-event periods (factor of 1.2 lower compared to
368 non-NPF mean), implying their necessity for growth. The sources and implications of these HOMs
369 are discussed in section 3.3. Further, concentrations of iodine and DMS-derived acids such as iodic
370 acid (HIO_3) and methanesulphonic acid (MSA) are low ($7.8 \cdot 10^5$ and $3.3 \cdot 10^5 \text{ cm}^{-3}$ respectively),
371 indicating a small influence of oceanic emissions on particle nucleation/growth. Extended box plots
372 as Figures 2 & 3 are presented in Figure S4, and HYSPLIT back trajectories per event in Figure S5.

373

374 **3.2 Mechanisms of New Particle Formation**

375 The correlation between $J_{1,9}$ and concentration of sulphuric acid is plotted in Figure 4. A close
376 relationship between nucleation rates and sulphuric acid concentrations ($R^2 = 0.49$) are consistent
377 with observations globally (Lee et al., 2019). This relationship is not dependent upon condensation
378 sink. These NPF rates have no dependence on other ions as measured by CI-Api-ToF, including
379 HIO_3 , MSA, ammonia, amines or HOMs (R^2 for all < 0.1). This is not to say that all of these
380 molecules are not involved in the nucleation process, rather that elevations or reductions to their
381 concentrations during nucleation periods do not have significant impact on nucleation rates. In the
382 example of alkylamines, their gas phase concentration may decrease due to clustering with elevated
383 sulphuric acid, as they cluster at around a 1:1 ratio at high amine mixing ratios (Kürten et al., 2014)
384 (and therefore they will not be detectable as free amines). Further, if amines are present at a few
385 pptv, their mixing ratios are significantly higher than our ambient measured sulphuric acid
386 concentrations, and will be sufficient to accelerate nucleation rates (Almeida et al., 2013).
387 Photochemical losses will also be greater during the periods of highest NPF rate (Ge et al., 2011b).
388 The strength of the relationship between sulphuric acid and nucleation rate has been quantitatively
389 reproduced in chamber studies involving the $\text{H}_2\text{SO}_4\text{-H}_2\text{O-DMA}$, and $\text{H}_2\text{SO}_4\text{-H}_2\text{O-BioOxOrg}$
390 system, accurately reproducing tropospheric observations of nucleation rates (Almeida et al., 2013;

391 Riccobono et al., 2014), although a later revision of the former shows nucleation rates at 278 K
392 exceeding typical tropospheric observations in the presence of high mixing ratios of DMA (Kürten
393 et al., 2018). A comparison between our data and results from the CLOUD chamber is presented in
394 Figure 5; included are the H₂SO₄-H₂O, H₂SO₄-NH₃-H₂O (Kirkby et al., 2011), H₂SO₄-H₂O-DMA
395 (Kürten et al., 2018) and H₂SO₄-BioOxOrg-H₂O systems (Riccobono et al., 2014) – BioOxOrg
396 refers to the oxidation products of pinanediol (C₁₀H₁₈O₂) and OH. Data from these chamber
397 experiments is for 278 K and 38 – 39 % relative humidity. Nucleation rates measured in Barcelona
398 ($J_{1.9} 178 \pm 190 \text{ cm}^{-3} \text{ s}^{-1}$ at $[\text{H}_2\text{SO}_4] 7.1 \cdot 10^6 \pm 2.7 \cdot 10^6 \text{ cm}^{-3}$) are around an order of magnitude lower
399 than that seen for the H₂SO₄-DMA-H₂SO₄ system, but exceed that of the H₂SO₄-BioOxOrg-H₂O
400 system by ~1 order of magnitude, and that of the H₂SO₄-NH₃-H₂O and H₂SO₄-H₂O system multiple
401 orders of magnitude. No dissimilarity is seen between the data points corresponding to full or burst
402 type nucleation, indicating similar mechanisms of formation, despite lower HOM concentrations on
403 burst-event days. Conversely, research in remote boreal environments show that the mechanism of
404 nucleation can modulate dependent upon the H₂SO₄:HOM ratio (Yan et al., 2018). Model studies of
405 sulphuric acid-amine nucleation show a decline in nucleation rate with an increasing temperature
406 (Almeida et al., 2013; Olenius et al., 2017), as the evaporation rate of sulphuric acid-amine clusters
407 will increase with temperature (Paasonen et al., 2012). Conversely, evaporation rates of such small
408 clusters, and resultant nucleation rates tend to increase modestly with increases in relative humidity,
409 most pronounced at lower amine concentrations (Almeida et al., 2013; Paasonen et al., 2012).
410 Despite this, high nucleation rates at temperatures nearing 300 K have been reported previously
411 (Kuang et al., 2008; Kürten et al., 2016), although these tend to show a temperature dependence
412 (Yu et al., 2016). No higher-order sulphuric acid clusters, sulphuric acid-base clusters, nor
413 sulphuric acid-HOM clusters were visible in the mass spectral data, likely due to these being below
414 the limit of detection of the instrument (Jokinen et al., 2012), so cluster identity cannot be directly
415 identified. Sulfuric acid trimer stabilisation is dependent upon base abundance (Ortega et al 2012),

416 and conversely, sensitivity of nitrate CI-API-ToF to sulfuric acid-base clusters is reduced due to the
417 high base content of such clusters (Jen et al., 2016).

418

419 To further explore the relationship between sulfuric acid clusters and the rate of nucleation, the
420 sulfuric acid dimer:monomer ratio is plotted in Figure 6. The sulfuric acid dimer:monomer ratio
421 is elevated by the presence of gas-phase bases such as DMA, and this elevation is dependent upon
422 both the abundances and proton affinities of such bases (Olenius et al., 2017). Upon charging,
423 evaporation of water and bases from sulfuric acid clusters occurs, and thus these are detected as
424 sulfuric acid dimer (Ortega et al., 2012, 2014). The binding energy of the bisulfate-H₂SO₄ ion is
425 in excess of 40 kcal mol⁻¹ (Curtius et al., 2001), and thus minimal declustering of the dimer is
426 expected within the CI-API-ToF instrument – however, declustering of higher order sulfuric acid
427 clusters has been shown to be sensitive to voltage tune (Passananti et al., 2019), and this likely
428 extends to the dimer also, and as such discrepancies between sets of results due to instrument setup
429 cannot be ruled out. The ratio of sulfuric acid dimer:monomer is also highly sensitive to
430 condensation sinks, with a difference in dimer concentration of approximately a factor of 4
431 expected at 10⁷ cm⁻³ between 0.001 s⁻¹ (a clean environment) and 0.03 s⁻¹ (condensation sinks
432 during these NPF events measured in this dataset) (Yao et al., 2018) and thus our low
433 dimer:monomer ratio can, in part, be explained by elevated condensation sinks. The dashed line
434 represents the ratio that would be seen due to ion induced clustering (IIC) in the nitrate chemical
435 ionisation system for a 50 ms reaction time (Zhao et al., 2010). The sulfuric acid dimer:monomer
436 ratio seen in the CLOUD H₂SO₄-DMA-H₂O system is plotted, alongside our own data from
437 Barcelona. The ratio from our own data is seen to be much lower than that for the system purely
438 involving DMA as a ternary stabilising species. Similarly, this ratio is lower than for reports of
439 H₂SO₄-DMA-H₂O nucleation in Shanghai (Yao et al., 2018), but is markedly similar to reports in
440 central rural Germany (Kürten et al., 2016). Similar to central Germany, this ratio increases at lower
441 sulfuric acid concentrations to a ratio more similar to the H₂SO₄-DMA-H₂O system. A possible

442 explanation for this is that at higher sulphuric acid concentrations, the concentrations of stronger
443 stabilising bases are insufficient to stabilise all present sulphuric acid, with the higher end of the
444 sulphuric acid concentrations seen in this data roughly equivalent to 1 pptv sulphuric acid (3×10^7
445 $\text{cm}^{-3} = 1.2$ pptv sulphuric acid). We also cannot account for clustering due to naturally charged
446 sulphuric acid in the atmosphere, but ion concentrations in urban environments tend to be small due
447 to efficient sink processes (Hirsikko et al., 2011). Particle formation plausibly operates by sulphuric
448 acid-amine nucleation involving the measured C₂ and C₄ amines in our data, with nucleation rates
449 hindered relative to those measured in the CLOUD experiments by elevated temperatures, and a
450 decline to the sulphuric acid dimer:monomer ratio indicates that base concentrations may be
451 limited. We cannot rule out an involvement of HOMs in particle formation processes, and, as no
452 higher-order clusters were observed, we cannot establish sulphuric acid-amine nucleation with
453 certainty.

454

455 **3.3 HOMs and Growth**

456 **3.3.1 HOM composition and sources**

457 Barcelona, as a densely populated urban agglomerate, is distinct from the remote conditions under
458 which HOMs have primarily been studied (Bianchi et al., 2016, 2017; Schobesberger et al., 2013;
459 Yan et al., 2016), and is characterised by elevated temperatures, insolation and NO_x mixing ratios,
460 as well as a diverse host of potential precursor VOC. The first of these affects HOM yields
461 significantly, as yields are highly dependent upon temperature (Quéléver et al., 2019; Stolzenburg et
462 al., 2018). Lower temperatures result in slower H-abstractions, which will result in the likelihood of
463 an RO₂ To undergo a different reaction pathway, such as termination with HO₂ To increase (Praske
464 et al., 2018). This is particularly important in this study if there is a large energy barrier for the first
465 or second H-abstraction taking place, as this will determine the number of hydrogen bond donating
466 groups, and therefore whether the NO₃⁻ CI-API-ToF is sensitive to a molecule or not. Elevated
467 insolation will result in enhanced photochemistry, and thus more rapid RO₂ Formation rates,

468 whereas elevated NO_x will produce more HOM with nitrate ester functionality (Garmash et al.,
469 2020; Rissanen, 2018), which tend towards higher volatilities, and less efficient participation in
470 particle formation (Ehn et al., 2014; Lehtipalo et al., 2018), and growth (Yan et al., 2020).

471

472 Oxygenated volatile organic compounds (OVOC) are defined as species visible in the nitrate CI-
473 ~~API~~-ToF that do not classify as HOM. Here, the first of the three criteria provided by Bianchi et
474 al. (2019), that HOM must be formed by peroxy radical autoxidation, cannot be applied to define
475 HOM, as knowledge as to whether a molecule is a result of autoxidation requires sound knowledge
476 of the structure of the precursors, oxidants and peroxy radical terminators present, however, the
477 number of molecules observed with $N_n = 2$ is around an order of magnitude lower than that for N_n
478 $N_n = 1$, where the primary source of multiple nitrogen functionalities would be multiple peroxy radical
479 termination reactions from NO_x, and therefore while multiple generations of oxidation have been
480 shown to occur in aromatics (Garmash et al., 2020), it is a small contributor to the concentration of
481 what is classed as HOM here. The second criterion to define HOM are that they must be formed in
482 the gas phase under atmospherically relevant conditions, which we deem appropriately fulfilled as all
483 ~~CI-API~~-ToF measurements are of gas phase compounds, and the final criterion is that HOM must
484 contain more than 6 oxygen atoms. To attempt to satisfy these criteria as best possible, the criteria of
485 both containing 6 oxygen atoms and 5 carbon atoms or greater and having an O:C ratio >0.6 is applied.

486

487 The diversified range of HOM precursors in Barcelona will be primarily anthropogenic in origin.
488 Averaged PTR-MS mixing ratios of different VOCs are presented in Figure S6. Figure 7(a) shows
489 HOM concentration plotted against temperature, showing a dependence of HOM concentrations on
490 temperature, with a lesser dependence on global radiation. The precursors for these HOMs are
491 presumed to be largely isoprene, alkylbenzenes, monoterpenes, and PAHs. The mean peak
492 intensities assigned to alkylbenzene derived HOMs are approximately a factor of two higher than
493 those assigned to isoprene and monoterpene oxidation across this entire campaign. In this data these

494 VOC mixing ratios are, with the exception of isoprene, not largely temperature dependent, with
495 many of these HOMs forming under negligible or zero insolation, and therefore very low OH
496 concentrations. These nighttime HOMs will not be derived from the oxidation of aromatics,
497 however, as rates of oxidation of alkylbenzenes by O_3 and NO_3 are negligible (Molteni et al.,
498 2018). These nighttime HOMs will therefore mostly be derived from biogenic emissions which
499 undergo more rapid nocturnal oxidation, and are likely transported from inland by the land breeze
500 during night (Millán, 2014; Querol et al., 2017).

501

502 Operating under the assumption that C_5 , C_6 , C_7 , C_8 , and C_9 HOMs primarily arise from isoprene,
503 benzene toluene, C_2 -alkylbenzene C_3 -alkylbenzene oxidation respectively (Massoli et al., 2018;
504 Molteni et al., 2018; Wang et al., 2017), HOM signals plotted against parent VOC concentration
505 indicate their dependence upon that VOC. Here, a C_7 HOM is thought to follow the formula C_7H_{8-}
506 $_{12}O_{5-10}N_{0-2}$. We have plotted HOM concentrations against VOC concentrations in Figure 7(b). C_{10}
507 HOMs are not included in these analyses as these may primarily arise from $C_{10}H_{12-14}$ alkylbenzene,
508 or monoterpene oxidation. HOM concentration appears mostly independent of VOC concentration,
509 with the exception of isoprene, for which emissions are highly temperature dependent, and thus this
510 is likely a function of the effect of temperature on HOM formation (Figure 7(a)). A lack of
511 correlation between other VOCs and their HOMs confirms that this relationship between HOMs
512 and temperature is not a function of enhanced VOC emission fluxes from, for example, evaporation,
513 except in the instance of isoprene. Fragmented monoterpene oxidation products will also contribute
514 to the total number of C_9 HOMs, and similarly, other VOCs can fragment upon oxidation. However,
515 these results indicate that HOM concentrations are elevated by temperature, and operate quite
516 independent of precursor VOC concentration.

517

518 DBE as calculated by equation 3 is equal to the number of pi bonds and rings within a molecule.
519 Benzene, toluene, and similar aromatics have $DBE = 4$, naphthalene = 7 and monoterpenes = 3.

520 DBE can be used as an indicator of sources when considering HOM in bulk. Saturation mass
521 concentration as calculated by equation 4 can help describe capacity of a molecule to both condense
522 onto newly formed particles and participate in nucleation. Figure 8 shows concentrations of HOMs
523 and other oxygenated organic molecules binned to the nearest integer $\text{Log}_{10}(C^*)(300\text{ K})$, coloured
524 by DBE. Mean ion signals per carbon number are shown in Figure S7. Most measured molecules
525 fall into the SVOC class ($0.3 < C^*(300\text{ K}) < 300\ \mu\text{g m}^{-3}$) which will mostly exist in equilibrium
526 between gas and particle phase. Highest SVOC concentrations arise from fingerprint molecules for
527 isoprene oxidation under high NO_x concentrations ($\text{C}_5\text{H}_{10}\text{N}_2\text{O}_8$) (Brean et al., [2019](#)[2020](#)), and
528 oxidation of small alkylbenzenes ($\text{C}_7\text{H}_8\text{O}_5$, $\text{C}_8\text{H}_{10}\text{O}_5$). LVOC and ELVOC ($3 \cdot 10^{-5} < C^* < 0.3\ \mu\text{g m}^{-3}$
529 and $3 \cdot 10^{-9} < C^*(300\text{ K}) < 3 \cdot 10^{-5}\ \mu\text{g m}^{-3}$ respectively) have a greater contribution from molecules
530 with higher DBE, i.e., $\text{C}_{10}\text{H}_{10}\text{O}_8$ arising most likely from PAH oxidation (Molteni et al., 2018), and
531 $\text{C}_{10}\text{H}_{15}\text{O}_7\text{N}$, a common molecule arising from monoterpene oxidation in the presence of NO_x . The
532 contribution of molecules with carbon number ≤ 9 to these LVOC is modest, and ELVOCs are
533 entirely comprised of molecules with carbon numbers ≥ 10 , and is dominated by DBEs of 8 and 4,
534 attributable to PAH and monoterpene oxidation respectively. No molecules classed as ultra-low
535 volatility organic compounds (ULVOC, $C^*(300\text{ K}) < 3 \cdot 10^{-9}\ \mu\text{g m}^{-3}$) were observed in our data, and
536 thus any pure HOM nucleation is unlikely.

537

538 3.3.2 HOMs and NPF

539 As shown in Figure 3, an elevated HOM concentration appears to be a necessary condition for particle
540 growth past 10 nm during NPF events. These days are associated with elevated temperatures, solar
541 radiation, higher ozone, and lower $\text{NO}:\text{NO}_2$ ratio. HIO_3 is also significantly higher on burst-event
542 days. A recent study in a remote environment reports growth rates matching condensation rates
543 without accounting for aqueous phase chemistry (Mohr et al., 2019). From 2D-VBS volatility
544 calculations discussed in the previous section, it is shown that LVOC and ELVOC measured in
545 Barcelona plausibly arise from the oxidation of aromatics (particularly PAHs in the case of ELVOC)

546 and monoterpenes. Calculated growth rates according to the method of Nieminen et al. (2010) are
547 presented in Figure S8 for both GR_{1.9-5} and GR₅₋₂₀. Best agreement for GR₅₋₂₀ is when condensation
548 of SVOC, LVOC, ELVOC, MSA, HIO₃ and H₂SO₄ is considered, and best agreement for GR_{1.9-5} is
549 seen for condensation of all these except SVOC. The uncertainties in this method are large, and
550 assumptions of irreversible condensation of SVOC onto particles of 5 nm likely lead to
551 overestimations; however, these results indicate an essential role of the condensation of organic
552 compounds to produce high growth rates observed in urban environments.

553

554 Figure 9 shows three mass-defect plots for a non-event period, full-event period, and burst-event
555 period. The non-event day included in Figure 8 was characterised by lower solar radiation and
556 temperatures than average, so lower signals for oxygenated species are seen due to weaker
557 photochemistry (i.e., OH[•] concentration), and slower autoxidation due to slower H-shift reactions
558 (Frege et al., 2018; Quéléver et al., 2019; Stolzenburg et al., 2018). The full-event day sees
559 enhancements to smaller OVOCs and HOMs compared to the non-event day, especially around
560 150-200 m/Q, which contains peaks corresponding to dicarboxylic acids and isoprene oxidation
561 products. Some of the largest peaks in the mass spectra correspond to formulae seen arising from
562 the enhanced OH[•] oxidation of alkylbenzenes (such as C₇H₇NO₆) (Molteni et al., 2018; Wang et al.,
563 2017). Larger HOMs see a less significant enhancement to smaller alkylbenzene derived HOMs.
564 The presence of larger, unidentified HOMs >400 m/Q is enhanced during full-events, these peaks
565 will comprise the largest compounds, most likely of class ELVOC, arising from the oxidation of
566 large VOCs, or RO₂[•]-RO₂[•] accretion reactions, and thus, we likely underpredict ELVOC
567 concentrations and resultant impacts on particle growth in Figure S8. These unidentified peaks
568 >400 m/Q are both more numerous and larger during full-event periods, with a factor of two
569 difference in total peak area. The burst-event day has significantly lower concentrations of OVOCs
570 and HOMs, and to a lesser degree, their nitrogen containing counterparts (N-OVOCs and N-
571 HOMs), with significantly fewer compounds >400 m/Q. The most significant difference between

572 full and burst-event days is in the SVOCs, accounting for a factor of two difference in
573 concentration. The sulphur containing acids all have similar peak areas to the full-event day. These
574 elevations to condensable OVOCs and HOMs on particle formation days with growth are consistent
575 with particle composition data as measured by ACSM (Figure S9). Particle composition on full-
576 event days shows an elevation to organic mass concentration in the late evening and night around
577 when new particles from NPF will reach sizes detectable by the ACSM (~75 nm, Ng et al., 2011).
578 Organic mass between 16:00 ~~and~~ 23:00 is $3.5 \mu\text{g m}^{-3}$ on burst-event days, versus $7.8 \mu\text{g m}^{-3}$ on
579 full-event days.

580

581 4. CONCLUSIONS

582 We show new particle formation rates in Barcelona are linearly dependent upon the sulphuric acid
583 concentrations, and while formation rates far exceed that of H_2SO_4 -BioOxOrg- H_2O nucleation, they
584 fall short of those of H_2SO_4 -DMA- H_2O nucleation at 278 K, as does the sulphuric acid
585 dimer:monomer ratio, possibly explained by cluster evaporation due to high temperatures in
586 summertime Barcelona (303 K during events), and limited pools of gas-phase amines. These results
587 are similar to reports of nucleation rates in rural Germany (Kürten et al., 2016). As no higher-order
588 clusters were directly measured, we cannot determine nucleation mechanisms with certainty, and an
589 involvement of HOMs in nucleation is plausible.

590

591 High concentrations of OVOCs and HOMs were measured by CI-APi-ToF. Of these, the SVOC
592 arose from mostly isoprene and alkylbenzene oxidation, whereas LVOC and ELVOC arose from
593 alkylbenzene, monoterpene and PAH oxidation together, with a dependence of their concentration
594 on temperature. Concentrations of species associated with coastal and oceanic sources such as MSA
595 and HIO_3 were low. High HOM ~~signals~~ concentrations are seen to be a necessary condition for new
596 particle growth past 10 nm, with the most significant difference between days with and without
597 particle growth being SVOC concentrations (factor of 2 difference), while modelled growth rates

598 from condensation of these organic compounds, alongside H₂SO₄, MSA and HIO₃ were shown to
599 match growth rates within measurement error. Thus, oxidation of traffic derived alkylbenzenes and
600 PAHs, and to a lesser degree, isoprene and monoterpene emissions is a significant determinant of
601 new particle growth in this environment.

602

603 These results are consistent with extensive chamber and flow tube studies on particle formation
604 from sulphuric acid, amines and HOMs, and further, nucleation rates relative to sulphuric acid are
605 similar to many tropospheric observations. Barcelona is representative of many Mediterranean
606 urban environments, with moderate pollution, influence of shipping emissions, and high insolation,
607 and the present study reveals the complexity of NPF mechanisms in these environments.

608

609 **DATA AVAILABILITY**

610 Data supporting this publication are openly available from the UBIRA eData repository at

611 <https://doi.org/10.25500/edata.bham.00000434>

612

613 **AUTHOR CONTRIBUTIONS**

614 RMH and XQ conceived the study, JB and DCSB carried out the CI-APi-TOF and related
615 measurements with assistance from AA and MCM. The VOC measurements were proposed by NM
616 and collected by BT-R. JB wrote the first draft of the manuscript which was enhanced by
617 contributions from the co-authors.

618

619 **COMPETING INTERESTS**

620 The authors have no conflict of interests.

621 **ACKNOWLEDGEMENTS**

622 Financial assistance from the Spanish Ministry of Science, Innovation and Universities and
623 Competitiveness and FEDER funds under the project HOUSE (CGL2016-78594-R), and by the
624 Generalitat de Catalunya (AGAUR 2017 SGR41) is gratefully acknowledged. MCM acknowledges
625 the Ramón y Cajal Fellowship awarded by the Spanish Ministry. Financial support of the UK
626 scientists by the Natural Environment Research Council through the National Centre for Atmospheric
627 Science is also acknowledged (R8/H12/83/011).

628

629 **FIGURE LEGENDS:**

630

631 **Figure 1:** Average SMPS contour plots for (a) non-event days, (b) full-event days and (c) burst-
632 event days.

633

634 **Figure 2:** Box plots for days of non-event, full-event and burst-event, showing (a) condensation
635 sink, (b) temperature, and (c) global radiation from hourly data. “Full-event” and “burst-
636 event” include data across the entire day.

637

638 **Figure 3:** Box plots for days of non-event, full-event and burst-event, showing (a) sulphuric acid,
639 (b) C₂ and C₄ amines, as clustered with the nitrate dimer and trimer, and (c) summed
640 HOM concentration from C₅₊ from hourly data. Units for ammonia + amines are
641 normalised counts, as no calibration was performed. Event days include data across the
642 full event day.

643

644 **Figure 4:** Formation rate (J_{1.9}) plotted against sulphuric acid monomer concentration, coloured by
645 condensation sink. Circles represent burst-events, squares represent full events. Data is
646 for hourly averages across NPF periods, typically within the hours 08:00 – 16:00. Slope
647 of the line = $4.9 \cdot 10^{-5} \text{ s}^{-1}$. Error bars represent systematic uncertainties on [H₂SO₄] and
648 J_{1.9}

649

650 **Figure 5:** Formation rate plotted against sulphuric acid monomer concentration for data collected
651 from Barcelona. Tan circles represent burst-events, purple squares represent full events.
652 as well as that for the H₂SO₄-H₂O (blue inverted triangles), H₂SO₄-NH₃-H₂O (yellow
653 inverted triangles), H₂SO₄-DMA-H₂O (pink triangles), and H₂SO₄-BioOxOrg-H₂O
654 (brown diamonds) systems from the CLOUD chamber (Kürten et al., 2018 Kirkby et al.,
655 2011; Riccobono et al., 2014). CLOUD chamber experiments were performed at 278 K
656 and 38 – 39 % RH. Data is for hourly averages across NPF periods, typically within the
657 hours 08:00 – 16:00. Error bars represent systematic uncertainties on [H₂SO₄] and J_{1.9}.

658

659 **Figure 6:** Sulphuric acid dimer concentration plotted against monomer concentration, showing
660 burst-event periods (tan circles), full event periods (purple squares), non-event periods
661 (green inverted triangles), and the ratio of sulphuric acid dimer:monomer in the CLOUD
662 chamber for the H₂SO₄-H₂O-DMA system (pink triangles) (Almeida et al., 2013).
663 Dashed line represents the dimer concentration produced by ion induced clustering in the
664 chemical ionization unit (Zhao et al., 2010). CLOUD chamber experiments were
665 performed at 278 K and 38 – 39 % RH. Data is for hourly averages across NPF periods,
666 typically within the hours 08:00 – 16:00. Error bars represent systematic uncertainties on
667 [H₂SO₄] and [(H₂SO₄)₂].

668

669 **Figure 7:** Influencing factors on HOM concentration, showing (a) C₅₋₁₀ HOM concentration plotted
670 against temperature, coloured by global radiation. Ellipsis shows 95% confidence on a
671 multivariate t-distribution. (b) HOM concentration by carbon number plotted against
672 parent VOC mixing ratio. These are segregated by carbon number/VOC, i.e. C₇ HOMs
673 plotted against toluene, under the assumption that toluene oxidation is the main producer
674 of C₇ HOMs. Time for both plots is of hourly time resolution.

675

676 **Figure 8:** Concentrations of all oxygenated organic molecules and HOMs binned to integer
677 Log₁₀(C*) values, coloured by DBE.

678

679 **Figure 9:** Mass defect plots for (a) non-event, (b) full-event, and (c) burst-event periods, data
680 taken from 10:00 – 15:00 on the days 11/07/2018, 16/07/2018 and 15/07/2018
681 respectively. Size corresponds to mass spectral peak area. Ions are coloured according
682 to identified chemical composition. *Blue* points correspond to HOMs containing all
683 organic species with ≥ 5 carbon atoms and ≥ 6 oxygen atoms, and an O:C ratio of >0.6 .
684 *Purple* points correspond to the same but for species containing 1-2 nitrogen atoms.
685 Species not meeting this HOM criteria were classed generally as OVOCs which are
686 coloured *brown*, with the nitrogen containing OVOCs coloured *orange*. Sulphur acids
687 (*red*) include ions HSO_4^- , CH_3SO_3^- and SO_5^- , as well as the sulphuric acid dimer. Iodine
688 acids (*green*) contains both IO_3^- and I^- (the latter presumably deprotonated hydrogen
689 iodide). Unidentified points are left uncoloured.
690
691

692 **REFERENCES**

693

694 Ábalos, M., Bayona, J. M. and Ventura, F.: Development of a solid-phase microextraction GC-NPD
695 procedure for the determination of free volatile amines in wastewater and sewage-polluted waters,
696 *Anal. Chem.*, 71(16), 3531–3537, doi:10.1021/ac990197h, 1999.

697

698 Almeida, J., Schobesberger, S., Kürten, A., Ortega, I. K., Kupiainen-Määttä, O., Praplan, A. P.,
699 Adamov, A., Amorim, A., Bianchi, F., Breitenlechner, M., David, A., Dommen, J., Donahue, N. M.,
700 Downard, A., Dunne, E., Duplissy, J., Ehrhart, S., Flagan, R. C., Franchin, A., Guida, R., Hakala, J.,
701 Hansel, A., Heinritzi, M., Henschel, H., Jokinen, T., Junninen, H., Kajos, M., Kangasluoma, J.,
702 Keskinen, H., Kupc, A., Kurtén, T., Kvashin, A. N., Laaksonen, A., Lehtipalo, K., Leiminger, M.,
703 Leppä, J., Loukonen, V., Makhmutov, V., Mathot, S., McGrath, M. J., Nieminen, T., Olenius, T.,
704 Onnela, A., Petäjä, T., Riccobono, F., Riipinen, I., Rissanen, M., Rondo, L., Ruuskanen, T., Santos,
705 F. D., Sarnela, N., Schallhart, S., Schnitzhofer, R., Seinfeld, J. H., Simon, M., Sipilä, M., Stozhkov,
706 Y., Stratmann, F., Tomé, A., Tröstl, J., Tsagkogeorgas, G., Vaattovaara, P., Viisanen, Y., Virtanen,
707 A., Vrtala, A., Wagner, P. E., Weingartner, E., Wex, H., Williamson, C., Wimmer, D., Ye, P., Yli-
708 Juuti, T., Carslaw, K. S., Kulmala, M., Curtius, J., Baltensperger, U., Worsnop, D. R., Vehkamäki,
709 H. and Kirkby, J.: Molecular understanding of sulphuric acid-amine particle nucleation in the
710 atmosphere, *Nature*, 502(7471), 359–363, doi:10.1038/nature12663, 2013.

711

712 Bianchi, F., Tröstl, J., Junninen, H., Frege, C., Henne, S., Hoyle, C. R., Molteni, U., Herrmann, E.,
713 Bukowiecki, N., Chen, X., Duplissy, J., Gysel, M., Hutterli, M., Kangasluoma, J., Kontkanen, J.,
714 Manninen, H. E., Münch, S., Peräkylä, O., Petäjä, T., Rondo, L., Williamson, C., Weingartner, E.,
715 Worsnop, D. R., Kulmala, M., Dommen, J. and Baltensperger, U.: New particle formation in the free
716 troposphere : A question of chemistry and timing, *Science* ~~(80-)~~, 5456(May), 1–11, 2016.

717

718 Bianchi, F., Garmash, O., He, X., Yan, C., Iyer, S., Rosendahl, I., Xu, Z., Rissanen, M. P., Riva, M.,
719 Taipale, R., Sarnela, N., Petäjä, T., Worsnop, D. R., Kulmala, M., Ehn, M. and Junninen, H.: The role
720 of highly oxygenated molecules (HOMs) in determining the composition of ambient ions in the boreal
721 forest, *Atmos. Chem. Phys.*, 17(22), 13819–13831, doi:10.5194/acp-17-13819-2017, 2017.

722

723 Bianchi, F., Kurtén, T., Riva, M., Mohr, C., Rissanen, M. P., Roldin, P., Berndt, T., Crouse, J. D.,
724 Wennberg, P. O., Mentel, T. F., Wildt, J., Junninen, H., Jokinen, T., Kulmala, M., Worsnop, D. R.,
725 Thornton, J. A., Donahue, N., Kjaergaard, H. G. and Ehn, M.: Highly Oxygenated Organic Molecules
726 (HOM) from Gas-Phase Autoxidation Involving Peroxy Radicals: A Key Contributor to Atmospheric
727 Aerosol, *Chem. Rev.*, 2019.

728

729 Bousiotis, D., Dall'osto, M., Beddows, D. C. S., Pope, F. D. and Harrison, R. M.: Analysis of new
730 particle formation (NPF) events at nearby rural, urban background and urban roadside sites, *Atmos.*
731 *Chem. Phys.*, 19, 5679–5694, doi:10.5194/acp-19-5679-2019, 2019.

732

733 [Brean, J., Harrison, R. M., Shi, Z., Beddows, D. C. S., Acton, W. J. F., Hewitt, C. N., Squires, F. A.,](#)
734 [and Lee, J.: Observations of highly oxidized molecules and particle nucleation in the atmosphere of](#)
735 [Beijing, *Atmos. Chem. Phys.*, 19, 14933–14947, <https://doi.org/10.5194/acp-19-14933-2019>,](#)
736 [2019.](#)~~[Brean, J., Harrison, R. M., Shi, Z., Beddows, D. C. S., W Joe, A. F. and Nicholas Hewitt, C.:](#)~~
737 ~~[Observations of highly oxidised molecules and particle nucleation in the atmosphere of Beijing,](#)~~
738 ~~[Atmos. Chem. Phys. Discuss.](#)~~, (March), 1–35, doi:10.5194/acp-2019-156, 2019.

739

740 Brines, M., Dall'Osto, M., Beddows, D. C. S., Harrison, R. M., and Querol, X.: Simplifying aerosol
741 size distributions modes simultaneously detected at four monitoring sites during SAPUSS, *Atmos.*
742 *Chem. Phys.*, 14, 2973–2986, <https://doi.org/10.5194/acp-14-2973-2014>, 2014.

743

744 Brines, M., Dall'Osto, M., Beddows, D. C. S., Harrison, R. M., Gómez-Moreno, F., Núñez, L.,
745 Artíñano, B., Costabile, F., Gobbi, G. P., Salimi, F., Morawska, L., Sioutas, C., and Querol, X.:
746 Traffic and nucleation events as main sources of ultrafine particles in high-insolation developed world
747 cities, *Atmos. Chem. Phys.*, 15, 5929–5945, <https://doi.org/10.5194/acp-15-5929-2015>, 2015.

748
749 Cadle, S. H. and Mulawa, P. A.: Low-molecular-weight aliphatic amines in exhaust from catalyst-
750 equipped cars, *Environ. Sci. Technol.*, 14(6), 718–723, doi:10.1021/es60166a011, 1980.

751
752 Carnerero, C., Pérez, N., Petäjä, T., Laurila, T. M., Ahonen, L. R., Kontkanen, J., Ahn, K. H.,
753 Alastuey, A. and Querol, X.: Relating high ozone, ultrafine particles, and new particle formation
754 episodes using cluster analysis, *Atmos. Environ. X*, 4(May), 1–20, doi:10.1016/j.aeaoa.2019.100051,
755 2019.

756
757 Cohen, A. J., Brauer, M., Burnett, R., Anderson, H. R., Frostad, J., Estep, K., Balakrishnan, K.,
758 Brunekreef, B., Dandona, L., Dandona, R., Feigin, V., Freedman, G., Hubbell, B., Jobling, A., Kan,
759 H., Knibbs, L., Liu, Y., Martin, R., Morawska, L., Pope, C. A., Shin, H., Straif, K., Shaddick, G.,
760 Thomas, M., van Dingenen, R., van Donkelaar, A., Vos, T., Murray, C. J. L. and Forouzanfar, M. H.:
761 Estimates and 25-year trends of the global burden of disease attributable to ambient air pollution: an
762 analysis of data from the Global Burden of Diseases Study 2015, *Lancet*, 389(10082), 1907–1918,
763 doi:10.1016/S0140-6736(17)30505-6, 2017.

764
765 Cubison, M. J. and Jimenez, J. L.: Statistical precision of the intensities retrieved from constrained
766 fitting of overlapping peaks in high-resolution mass spectra, *Atmos. Meas. Tech.*, 8(6), 2333–2345,
767 doi:10.5194/amt-8-2333-2015, 2015.

768
769 Curtius, J., Froyd, K. D. and Lovejoy, E. R.: Cluster ion thermal decomposition (I): Experimental
770 kinetics study and ab initio calculations for $\text{HSO}_4^-(\text{H}_2\text{SO}_4)_x(\text{HNO}_3)_y$, *J. Phys. Chem. A*, 105(48),
771 10867–10873, doi:10.1021/jp0124950, 2001.

772
773 Dal Maso, M., Kulmala, M., Riipinen, I., Wagner, R., Hussein, T., Aalto, P. P. and Lehtinen, K. E.
774 J.: Formation and growth of fresh atmospheric aerosols: Eight years of aerosol size distribution data
775 from SMEAR II, Hyytiälä, Finland, *Boreal Environ. Res.*, 10(5), 323–336, 2005.

776
777 Dall'Osto, M., Querol, X., Alastuey, A., O'Dowd, C., Harrison, R. M., Wenger, J. and Gómez-
778 Moreno, F. J.: On the spatial distribution and evolution of ultrafine particles in Barcelona, *Atmos.*
779 *Chem. Phys.*, 13(2), 741–759, doi:10.5194/acp-13-741-2013, 2013.

780
781 Donahue, N. M., Epstein, S. A., Pandis, S. N. and Robinson, A. L.: Atmospheric Chemistry and
782 Physics A two-dimensional volatility basis set: 1. organic-aerosol mixing thermodynamics, *Atmos.*
783 *Chem. Phys.*, 11, 3303–3318, doi:10.5194/acp-11-3303-2011, 2011.

784
785 Ehn, M., Thornton, J. A., Kleist, E., Sipilä, M., Junninen, H., Pullinen, I., Springer, M., Rubach, F.,
786 Tillmann, R., Lee, B., Lopez-Hilfiker, F., Andres, S., Acir, I.-H., Rissanen, M., Jokinen, T.,
787 Schobesberger, S., Kangasluoma, J., Kontkanen, J., Nieminen, T., Kurtén, T., Nielsen, L. B.,
788 Jørgensen, S., Kjaergaard, H. G., Canagaratna, M., Maso, M. D., Berndt, T., Petäjä, T., Wahner, A.,
789 Kerminen, V.-M., Kulmala, M., Worsnop, D. R., Wildt, J. and Mentel, T. F.: A large source of low-
790 volatility secondary organic aerosol, *Nature*, 506(7489), 476–479, doi:10.1038/nature13032, 2014.

791
792 Elm, J., Myllys, N. and Kurtén, T.: What is Required for Highly Oxidized Molecules to Form Clusters
793 with Sulphuric Acid?, *J. Phys. Chem. A*, 121(23), 4578–4587, doi:10.1021/acs.jpca.7b03759, 2017.

794
795 Frege, C., Ortega, I. K., Rissanen, M. P., Praplan, A. P., Steiner, G., Heinritzi, M., Ahonen, L.,

796 Amorim, A., Bernhammer, A. K., Bianchi, F., Brilke, S., Breitenlechner, M., Dada, L., Dias, A.,
797 Duplissy, J., Ehrhart, S., El-Haddad, I., Fischer, L., Fuchs, C., Garmash, O., Gonin, M., Hansel, A.,
798 Hoyle, C. R., Jokinen, T., Junninen, H., Kirkby, J., Kürten, A., Lehtipalo, K., Leiminger, M., Lee
799 Mauldin, R., Molteni, U., Nichman, L., Petäjä, T., Sarnela, N., Schobesberger, S., Simon, M., Sipilä,
800 M., Stolzenburg, D., Tomé, A., Vogel, A. L., Wagner, A. C., Wagner, R., Xiao, M., Yan, C., Ye, P.,
801 Curtius, J., Donahue, N. M., Flagan, R. C., Kulmala, M., Worsnop, D. R., Winkler, P., Dommen, J.
802 and Baltensperger, U.: Influence of temperature on the molecular composition of ions and charged
803 clusters during pure biogenic nucleation, *Atmos. Chem. Phys.*, 18(1), 65–79, doi:10.5194/acp-18-65-
804 2018, 2018.

805

806 Garmash, O., Rissanen, M. P., Pullinen, I., Schmitt, S., Kausiala, O., Tillmann, R., Zhao, D., Percival,
807 C., Bannan, T. J., Priestley, M., Hallquist, Å. M., Kleist, E., Kiendler-Scharr, A., Hallquist, M.,
808 Berndt, T., McFiggans, G., Wildt, J., Mentel, T. F., and Ehn, M.: Multi-generation OH oxidation as
809 a source for highly oxygenated organic molecules from aromatics, *Atmos. Chem. Phys.*, 20, 515–
810 537, doi:10.5194/acp-20-515-2020, 2020.

811

812 Ge, X., Wexler, A. S. and Clegg, S. L.: Atmospheric amines — Part I. A review, *Atmos. Environ.*,
813 45(3), 524–546, doi:10.1016/j.atmosenv.2010.10.012, 2011a.

814

815 Ge, X., Wexler, A. S. and Clegg, S. L.: Atmospheric amines — Part II. Thermodynamic properties
816 and gas/particle partitioning, *Atmos. Environ.*, 45(3), 561–577, doi:10.1016/j.atmosenv.2010.10.013,
817 2011b.

818

819 ~~Glasee, W. A., Volz, K., Panta, B., Freshour, N., Bachman, R., Hanson, D. R., Memurly, P. H. and~~
820 ~~Jen, C.: Sulphuric acid nucleation: An experimental study of the effect of seven bases, *J. Geophys.*~~
821 ~~*Res. Atmos.*, 175(120), 1933–1950, doi:10.1038/175238e0, 2015.~~

822

823 Graus, M., Müller, M. and Hansel, A.: High resolution PTR-TOF: Quantification and Formula
824 Confirmation of VOC in Real Time, *J. Am. Soc. Mass Spectrom.*, 21(6), 1037–1044,
825 doi:10.1016/j.jasms.2010.02.006, 2010.

826

827 Guo, S., Hu, M., Zamora, M. L., Peng, J., Shang, D., Zheng, J., Du, Z., Wu, Z., Shao, M., Zeng, L.,
828 Molina, M. J. and Zhang, R.: Elucidating severe urban haze formation in China., *Proc. Natl. Acad.*
829 *Sci. U. S. A.*, 111(49), 17373–8, doi:10.1073/pnas.1419604111, 2014.

830

831 Harrison, R. M., Rob Mackenzie, A., Xu, H., Alam, M. S., Nikolova, I., Zhong, J., Singh, A., Zeraati-
832 Rezaei, S., Stark, C., Beddows, D. C. S., Liang, Z., Xu, R. and Cai, X.: Diesel exhaust nanoparticles
833 and their behaviour in the atmosphere, *Proc. R. Soc. A Math. Phys. Eng. Sci.*, 474(2220),
834 doi:10.1098/rspa.2018.0492, 2018.

835

836 Henschel, S., Querol, X., Atkinson, R., Pandolfi, M., Zeka, A., Tertre, A. L., Analitis, A.,
837 Katsouyanni, K., Chanel, O., Pascal, M., Bouland, C., Haluza, D., Medina, S., and Goodman, P. G.:
838 Ambient air SO₂ patterns in 6 European cities, *Atmos. Environ.*, 79, 236–247,
839 doi:10.1016/j.atmosenv.2013.06.008, 2013.

840

841 Hirsikko, A., Nieminen, T., Gagné, S., Lehtipalo, K., Manninen, H. E., Ehn, M., Hörrak, U.,
842 Kerminen, V.-M., Laakso, L., Mcmurry, P. H., Mirme, A., Mirme, S., Petäjä, T., Tammet, H.,
843 Vakkari, V., Vana, M. and Kulmala, M.: Atmospheric ions and nucleation: a review of observations,
844 *Atmos. Chem. Phys.*, 11, 767–798, doi:10.5194/acp-11-767-2011, 2011.

845

846 Hutchinson, G. L., Mosier, A. R. and Andre, C. E.: Ammonia and Amine Emissions from a Large

847 Cattle Feedlot, *J. Environ. Qual.*, 11(2), 288–293, 1982.
848

849 Hyttinen, N., Kupiainen-Määttä, O., Rissanen, M. P., Muuronen, M., Ehn, M. and Kurtén, T.:
850 Modeling the Charging of Highly Oxidized Cyclohexene Ozonolysis Products Using Nitrate-Based
851 Chemical Ionization, *J. Phys. Chem. A*, 119(24), 6339–6345, doi:10.1021/acs.jpca.5b01818, 2015.
852

853 IPCC, 2013: Climate Change 2013: The Physical Science Basis. Contribution of Working Group I to
854 the Fifth Assessment Report of the Intergovernmental Panel on Climate Change, edited by V. B. and
855 P. M. M. Stocker, T.F., D. Qin, G.-K. Plattner, M. Tignor, S.K. Allen, J. Boschung, A. Nauels, Y.
856 Xia, Cambridge University Press, Cambridge., 2014.
857

858 Jen, C. N., Zhao, J., McMurry, P. H., and Hanson, D. R.: Chemical ionization of clusters formed from
859 sulfuric acid and dimethylamine or diamines, *Atmos. Chem. Phys.*, 16, 12513–12529,
860 doi:10.5194/acp-16-12513-2016, 2016.
861

862 Jokinen, T., Sipilä, M., Junninen, H., Ehn, M., Lönn, G., Hakala, J., Petäjä, T., Mauldin, R. L.,
863 Kulmala, M. and Worsnop, D. R.: Atmospheric sulphuric acid and neutral cluster measurements using
864 CI-API-TOF, *Atmos. Chem. Phys.*, 12(9), 4117–4125, doi:10.5194/acp-12-4117-2012, 2012.
865

866 Jokinen, T., Sipilä, M., Kontkanen, J., Vakkari, V., Tisler, P., Duplissy, E.-M., Junninen, H.,
867 Kangasluoma, J., Manninen, H. E., Petäjä, T., Kulmala, M., Worsnop, D. R., Kirkby, J., Virkkula, A.
868 and Kerminen, V.-M.: Ion-induced sulphuric acid–ammonia nucleation drives particle formation in
869 coastal Antarctica, *Sci. Adv.*, 4(11), eaat9744, doi:10.1126/sciadv.aat9744, 2018.
870

871 Junninen, H., Ehn, M., Petäjä, Luosujärvi, L., Kotiaho, T., Kostianen, R., Rohner, U., Gonin, M.,
872 Fuhrer, K., Kulmala, M. and Worsnop, D. R.: A high-resolution mass spectrometer to measure
873 atmospheric ion composition, *Atmos. Meas. Tech.*, 3(4), 1039–1053, doi:10.5194/amt-3-1039-2010,
874 2010.
875

876 Kerminen, V. M., Chen, X., Vakkari, V., Petäjä, T., Kulmala, M. and Bianchi, F.: Atmospheric new
877 particle formation and growth: Review of field observations, *Environ. Res. Lett.*, 13(10),
878 doi:10.1088/1748-9326/aadf3c, 2018.
879

880 Kirkby, J., Curtius, J., Almeida, J., Dunne, E., Duplissy, J., Ehrhart, S., Franchin, A., Gagné, S., Ickes,
881 L., Kürten, A., Kupc, A., Metzger, A., Riccobono, F., Rondo, L., Schobesberger, S., Tsagkogeorgas,
882 G., Wimmer, D., Amorim, A., Bianchi, F., Breitenlechner, M., David, A., Dommen, J., Downard, A.,
883 Ehn, M., Flagan, R. C., Haider, S., Hansel, A., Hauser, D., Jud, W., Junninen, H., Kreissl, F., Kvashin,
884 A., Laaksonen, A., Lehtipalo, K., Lima, J., Lovejoy, E. R., Makhmutov, V., Mathot, S., Mikkilä, J.,
885 Minginette, P., Mogo, S., Nieminen, T., Onnela, A., Pereira, P., Petäjä, T., Schnitzhofer, R., Seinfeld,
886 J. H., Sipilä, M., Stozhkov, Y., Stratmann, F., Tomé, A., Vanhanen, J., Viisanen, Y., Vrtala, A.,
887 Wagner, P. E., Walther, H., Weingartner, E., Wex, H., Winkler, P. M., Carslaw, K. S., Worsnop, D.
888 R., Baltensperger, U. and Kulmala, M.: Role of sulphuric acid, ammonia and galactic cosmic rays in
889 atmospheric aerosol nucleation, *Nature*, 476(7361), 429–435, doi:10.1038/nature10343, 2011.
890

891 Kirkby, J., Duplissy, J., Sengupta, K., Frege, C., Gordon, H., Williamson, C., Heinritzi, M., Simon,
892 M., Yan, C., Almeida, J., Trostl, J., Nieminen, T., Ortega, I. K., Wagner, R., Adamov, A., Amorim,
893 A., Bernhammer, A. K., Bianchi, F., Breitenlechner, M., Brilke, S., Chen, X., Craven, J., Dias, A.,
894 Ehrhart, S., Flagan, R. C., Franchin, A., Fuchs, C., Guida, R., Hakala, J., Hoyle, C. R., Jokinen, T.,
895 Junninen, H., Kangasluoma, J., Kim, J., Krapf, M., KürtenKurten, A., Laaksonen, A., Lehtipalo, K.,
896 Makhmutov, V., Mathot, S., Molteni, U., Onnela, A., Perakyla, O., Piel, F., Petaja, T., Praplan, A. P.,
897 Pringle, K., Rap, A., Richards, N. A. D., Riipinen, I., Rissanen, M. P., Rondo, L., Sarnela, N.,
898 Schobesberger, S., Scott, C. E., Seinfeld, J. H., Sipilä, M., Steiner, G., Stozhkov, Y., Stratmann, F.,

899 Tomé, A., Virtanen, A., Vogel, A. L., Wagner, A. C., Wagner, P. E., Weingartner, E., Wimmer, D.,
900 Winkler, P. M., Ye, P., Zhang, X., Hansel, A., Dommen, J., Donahue, N. M., Worsnop, D. R.,
901 Baltensperger, U., Kulmala, M., Carslaw, K. S. and Curtius, J.: Ion-induced nucleation of pure
902 biogenic particles, *Nature*, 533(7604), 521–526, doi:10.1038/nature17953, 2016.
903
904 Kuang, C., McMurry, P. H., McCormick, A. V. and Eisele, F. L.: Dependence of nucleation rates on
905 sulfuric acid vapor concentration in diverse atmospheric locations, *J. Geophys. Res. Atmos.*, 113(10),
906 1–9, doi:10.1029/2007JD009253, 2008.
907
908 Kulmala, M., Dal Maso, M., Mäkelä, J. M., Pirjola, L., Väkevä, M., Aalto, P., Miikkulainen, P.,
909 Hämeri, K. and O’Dowd, C. D.: On the formation, growth and composition of nucleation mode
910 particles, *Tellus, Ser. B Chem. Phys. Meteorol.*, 53(4), 479–490, doi:10.1034/j.1600-0889.2001.d01-
911 33.x, 2001.
912
913 Kulmala, M., Petäjä, T., Nieminen, T., Sipilä, M., Manninen, H. E., Lehtipalo, K., Dal Maso, M.,
914 Aalto, P. P., Junninen, H., Paasonen, P., Riiipinen, I., Lehtinen, K. E. J., Laaksonen, A. and Kerminen,
915 V.-M.: Measurement of the nucleation of atmospheric aerosol particles, *Nat. Protoc.*, 7(9), 1651–
916 1667, doi:10.1038/nprot.2012.091, 2012.
917
918 Kulmala, M., Kerminen, V. M., Petäjä, T., Ding, A. J. and Wang, L.: Atmospheric gas-to-particle
919 conversion: Why NPF events are observed in megacities?, *Faraday Discuss.*, 200, 271–288,
920 doi:10.1039/c6fd00257a, 2017.
921
922 Kürten, A., Jokinen, T., Simon, M., Sipilä, M., Sarnela, N., Junninen, H., Adamov, A., Almeida, J.,
923 Amorim, A., Bianchi, F., Breitenlechner, M., Dommen, J., Donahue, N. M., Duplissy, J., Ehrhart, S.,
924 Flagan, R. C., Franchin, A., Hakala, J., Hansel, A., Heinritzi, M., Hutterli, M., Kangasluoma, J.,
925 Kirkby, J., Laaksonen, A., Lehtipalo, K., Leiminger, M., Makhmutov, V., Mathot, S., Onnela, A.,
926 Petäjä, T., Praplan, A. P., Riccobono, F., Rissanen, M. P., Rondo, L., Schobesberger, S., Seinfeld, J.
927 H., Steiner, G., Tomé, A., Tröstl, J., Winkler, P. M., Williamson, C., Wimmer, D., Ye, P.,
928 Baltensperger, U., Carslaw, K. S., Kulmala, M., Worsnop, D. R. and Curtius, J.: Neutral molecular
929 cluster formation of sulfuric acid–dimethylamine observed in real time under atmospheric conditions,
930 *Proc. Natl. Acad. Sci.*, 111(42), 15019–15024, doi:10.1073/pnas.1404853111, 2014.
931
932 Kürten, A., Münch, S., Rondo, L., Bianchi, F., Duplissy, J., Jokinen, T., Junninen, H., Sarnela, N.,
933 Schobesberger, S., Simon, M., Sipilä, M., Almeida, J., Amorim, A., Dommen, J., Donahue, N. M.,
934 Dunne, E. M., Flagan, R. C., Franchin, A., Kirkby, J., Kupc, A., Makhmutov, V., Petäjä, T., Praplan,
935 A. P., Riccobono, F., Steiner, G., Tomé, A., Tsagkogeorgas, G., Wagner, P. E., Wimmer, D.,
936 Baltensperger, U., Kulmala, M., Worsnop, D. R. and Curtius, J.: Thermodynamics of the formation
937 of sulfuric acid dimers in the binary (H₂SO₄-H₂O) and ternary (H₂SO₄-H₂O-NH₃) system, *Atmos.*
938 *Chem. Phys.*, 15(18), 10701–10721, doi:10.5194/acp-15-10701-2015, 2015.
939
940 Kürten, A., Bergen, A., Heinritzi, M., Leiminger, M., Lorenz, V., Piel, F., Simon, M., Sitals, R.,
941 Wagner, A. C. and Curtius, J.: Observation of new particle formation and measurement of sulphuric
942 acid, ammonia, amines and highly oxidized organic molecules at a rural site in central Germany,
943 *Atmos. Chem. Phys.*, 16(19), 12793–12813, doi:10.5194/acp-16-12793-2016, 2016.
944
945 Kürten, A., Li, C., Bianchi, F., Curtius, J., Dias, A., Donahue, N. M., Duplissy, J., Flagan, R. C.,
946 Hakala, J., Jokinen, T., Kirkby, J., Kulmala, M., Laaksonen, A., Lehtipalo, K., Makhmutov, V.,
947 Onnela, A., Rissanen, M. P., Simon, M., Sipilä, M., Stozhkov, Y., Tröstl, J., Ye, P. and McMurry, P.
948 H.: New particle formation in the sulfuric acid-dimethylamine-water system: Reevaluation of
949 CLOUD chamber measurements and comparison to an aerosol nucleation and growth model, *Atmos.*
950 *Chem. Phys.*, 18(2), 845–863, doi:10.5194/acp-18-845-2018, 2018.

951

952 Kurtén, T., Noppel, M., Vehkamäki, H., Salonen, M. and Kulmala, M.: Quantum chemical studies of
953 hydrate formation of H₂SO₄ and HSO₄⁻, *Boreal Environ. Res.*, 12(3), 431–453, 2007.

954

955 Kurtén, T., Loukonen, V., Vehkamäki, H. and Kulmala, M.: Amines are likely to enhance neutral and
956 ion-induced sulphuric acid-water nucleation in the atmosphere more effectively than ammonia,
957 *Atmos. Chem. Phys.*, 8(14), 4095–4103, doi:10.5194/acp-8-4095-2008, 2008.

958

959

960 Lee, S. H., Gordon, H., Yu, H., Lehtipalo, K., Haley, R., Li, Y. and Zhang, R.: New Particle Formation
961 in the Atmosphere: From Molecular Clusters to Global Climate, *J. Geophys. Res. Atmos.*,
962 doi:10.1029/2018JD029356, 2019.

963

964 [Lehtinen, K. E. J., Dal Maso, M., Kulmala, M. and Kerminen, V. M.: Estimating nucleation rates](#)
965 [from apparent particle formation rates and vice versa: Revised formulation of the Kerminen-Kulmala](#)
966 [equation, *J. Aerosol Sci.*, 38\(9\), 988–994, doi:10.1016/j.jaerosci.2007.06.009, 2007.](#)

967

968 Lehtinen, K. E. J., Dal Maso, M., Kulmala, M. and Kerminen, V. M.: Estimating nucleation rates
969 from apparent particle formation rates and vice versa: Revised formulation of the Kerminen-Kulmala
970 equation, *J. Aerosol Sci.*, 38(9), 988–994, doi:10.1016/j.jaerosci.2007.06.009, 2007.

971

972 Lehtipalo, K., Yan, C., Dada, L., Bianchi, F., Xiao, M., Wagner, R., Stolzenburg, D., Ahonen, L. R.,
973 Amorim, A., Baccarini, A., Bauer, P. S., Baumgartner, B., Bergen, A., Bernhammer, A.-K.,
974 Breitenlechner, M., Brilke, S., Buchholz, A., Mazon, S. B., Chen, D., Chen, X., Dias, A., Dommen,
975 J., Draper, D. C., Duplissy, J., Ehn, M., Finkenzeller, H., Fischer, L., Frege, C., Fuchs, C., Garmash,
976 O., Gordon, H., Hakala, J., He, X., Heikkinen, L., Heinritzi, M., Helm, J. C., Hofbauer, V., Hoyle, C.
977 R., Jokinen, T., Kangasluoma, J., Kerminen, V.-M., Kim, C., Kirkby, J., Kontkanen, J., Kürten, A.,
978 Lawler, M. J., Mai, H., Mathot, S., Mauldin, R. L., Molteni, U., Nichman, L., Nie, W., Nieminen, T.,
979 Ojdanic, A., Onnela, A., Passananti, M., Petäjä, T., Piel, F., Pospisilova, V., Quéléver, L. L. J.,
980 Rissanen, M. P., Rose, C., Sarnela, N., Schallhart, S., Schuchmann, S., Sengupta, K., Simon, M.,
981 Sipilä, M., Tauber, C., Tomé, A., Tröstl, J., Väisänen, O., Vogel, A. L., Volkamer, R., Wagner, A.
982 C., Wang, M., Weitz, L., Wimmer, D., Ye, P., Ylisirniö, A., Zha, Q., Carslaw, K. S., Curtius, J.,
983 Donahue, N. M., Flagan, R. C., Hansel, A., Riipinen, I., Virtanen, A., Winkler, P. M., Baltensperger,
984 U., Kulmala, M. and Worsnop, D. R.: Multicomponent new particle formation from sulphuric acid,
985 ammonia, and biogenic vapors, *Sci. Adv.*, 4(12), eaau5363, doi:10.1126/sciadv.aau5363, 2018.

986

987 Massoli, P., Stark, H., Canagaratna, M. R., Krechmer, J. E., Xu, L., Ng, N. L., Mauldin, R. L., Yan,
988 C., Kimmel, J., Misztal, P. K., Jimenez, J. L., Jayne, J. T. and Worsnop, D. R.: Ambient
989 Measurements of Highly Oxidized Gas-Phase Molecules during the Southern Oxidant and Aerosol
990 Study (SOAS) 2013, *ACS Earth Sp. Chem.*, 2(7), 653–672,
991 doi:10.1021/acsearthspacechem.8b00028, 2018.

992

993 Mikkonen, S., Romakkaniemi, S., Smith, J. N., Korhonen, H., Petäjä, T., Plass-Duelmer, C., Boy, M.,
994 McMurry, P. H., Lehtinen, K. E. J., Joutsensaari, J., Hamed, A., Mauldin, R. L., Birmili, W., Spindler,
995 G., Arnold, F., Kulmala, M. and Laaksonen, A.: A statistical proxy for sulphuric acid concentration,
996 *Atmos. Chem. Phys.*, 11(21), 11319–11334, doi:10.5194/acp-11-11319-2011, 2011.

997

998 Millán, M.: Extreme hydrometeorological events and climate change predictions in Europe, *J.*
999 *Hydrol.*, 518(PB), 206–224, doi:10.1016/j.jhydrol.2013.12.041, 2014.

1000

1001 Miller, M. R., Raftis, J. B., Langrish, J. P., McLean, S. G., Samutrtai, P., Connell, S. P., Wilson, S.,
1002 Vesey, A. T., Fokkens, P. H. B., Boere, A. J. F., Krystek, P., Campbell, C. J., Hadoke, P. W. F.,

1003 Donaldson, K., Cassee, F. R., Newby, D. E., Duffin, R. and Mills, N. L.: Inhaled Nanoparticles
1004 Accumulate at Sites of Vascular Disease, *ACS Nano*, 11(5), 4542–4552,
1005 doi:10.1021/acsnano.6b08551, 2017.

1006

1007 Minguillón, M. C., Brines, M., Pérez, N., Reche, C., Pandol, M., Fonseca, A. S., Amato, F., Alastuey,
1008 A., Lyasota, A., Codina, B., Lee, H., Eun, H., Ahn, K. and Querol, X.: New particle formation at
1009 ground level and in the vertical column over the Barcelona area, *—*, 165, 118–130,
1010 doi:10.1016/j.atmosres.2015.05.003, 2015.

1011

1012

1013 Minguillón, M.C., Pérez, N., Marchand, N., Bertrand, A., Temime-Roussel, B., Agrios, K., Szidat,
1014 S., van Drooge, B.L., Sylvestre, A., Alastuey, A., Reche, C., Ripoll, A., Marco, E., Grimalt, J.O.,
1015 Querol, X.: Secondary organic aerosol origin in an urban environment. Influence of biogenic and fuel
1016 combustion precursors. *Faraday Discuss.*, 189, 337–359, 2016.

1017

1018 Mohr, C., Thornton, J. A., Heitto, A., Lopez-Hilfiker, F. D., Lutz, A., Riipinen, I., Hong, J., Donahue,
1019 N. M., Hallquist, M., Petäjä, T., Kulmala, M. and Yli-Juuti, T.: Molecular identification of organic
1020 vapors driving atmospheric nanoparticle growth, *Nat. Commun.*, 10(1), 1–7, doi:10.1038/s41467-
1021 019-12473-2, 2019.

1022

1023 Møller, K. H., Tram, C. M. and Kjaergaard, H. G.: Side-by-Side Comparison of Hydroperoxide and
1024 Corresponding Alcohol as Hydrogen-Bond Donors, *J. Phys. Chem. A*, 121(15), 2951–2959,
1025 doi:10.1021/acs.jpca.7b01323, 2017.

1026

1027 Molteni, U., Bianchi, F., Klein, F., El Haddad, I., Frege, C., Rossi, M. J., Dommen, J. and
1028 Baltensperger, U.: Formation of highly oxygenated organic molecules from aromatic compounds,
1029 *Atmos. Chem. Phys.*, 18(3), 1909–1921, doi:10.5194/acp-18-1909-2018, 2018.

1030

1031 Ng, N. L., Herndon, S. C., Trimborn, A., Canagaratna, M. R., Croteau, P. L., Onasch, T. B., Sueper,
1032 D., Worsnop, D. R., Zhang, Q., Sun, Y. L. and Jayne, J. T.: An Aerosol Chemical Speciation Monitor
1033 (ACSM) for routine monitoring of the composition and mass concentrations of ambient aerosol,
1034 *Aerosol Sci. Technol.*, 45(7), 770–784, doi:10.1080/02786826.2011.560211, 2011.

1035

1036 [Nieminen, T., Lehtinen, K. E. J., and Kulmala, M.: Sub-10 nm particle growth by vapor condensation](#)
1037 [– effects of vapor molecule size and particle thermal speed, *Atmos. Chem. Phys.*, 10, 9773–9779,](#)
1038 [doi:10.5194/acp-10-9773-2010, 2010](#)

1039

1040 Olenius, T., Halonen, R., Kurtén, T., Henschel, H., Kupiainen-Määttä, O., Ortega, I. K., Jen, C. N.,
1041 Vehkamäki, H. and Riipinen, I.: New particle formation from sulfuric acid and amines: Comparison
1042 of monomethylamine, dimethylamine, and trimethylamine, *J. Geophys. Res.*, 122(13), 7103–7118,
1043 doi:10.1002/2017JD026501, 2017.

1044

1045 Olin, M., Kuuluvainen, H., Aurela, M., Kalliokoski, J., Kuittinen, N., Isotalo, M., Timonen, H. J.,
1046 Niemi, J. V., Rönkkö, T., and Dal Maso, M.: Traffic-originated nanocluster emission exceeds H₂SO₄-
1047 driven photochemical new particle formation in an urban area, *Atmos. Chem. Phys.*, 20, 1–13,
1048 <https://doi.org/10.5194/acp-20-1-2020>, 2020.

1049

1050 Ortega, I. K., Olenius, T., Kupiainen-Määttä, O., Loukonen, V., Kurtén, T., and Vehkamäki, H.:
1051 Electrical charging changes the composition of sulfuric acid–ammonia/dimethylamine clusters,
1052 *Atmos. Chem. Phys.*, 14, 7995–8007, <https://doi.org/10.5194/acp-14-7995-2014>, 2014.

1053

1054 Paasonen, P., Olenius, T., Kupiainen, O., Kurtén, T., Petäjä, T., Birmili, W., Hamed, A., Hu, M.,

1055 Huey, L. G., Plass-Duelmer, C., Smith, J. N., Wiedensohler, A., Loukonen, V., McGrath, M. J.,
1056 Ortega, I. K., Laaksonen, A., Vehkamäki, H. and Kulmala, M.: On the formation of sulphuric acid
1057 – Amine clusters in varying atmospheric conditions and its influence on atmospheric new
1058 particle formation, *Atmos. Chem. Phys.*, 12(19), 9113–9133, doi:10.5194/acp-12-9113-2012, 2012.
1059

1060 Pandolfi, M., Amato, F., Reche, C., Alastuey, A., Otjes, R. P., Blom, M. J. and Querol, X.: Summer
1061 ammonia measurements in a densely populated Mediterranean city, *Atmos. Chem. Phys.*, 12(16),
1062 7557–7575, doi:10.5194/acp-12-7557-2012, 2012.
1063

1064 Passananti, M., Zapadinsky, E., Zanca, T., Kangasluoma, J., Myllys, N., Rissanen, M. P., Kurtén, T.,
1065 Ehn, M., Attoui, M. and Vehkamäki, H.: How well can we predict cluster fragmentation inside a mass
1066 spectrometer?, *Chem. Commun.*, 55(42), 5946–5949, doi:10.1039/c9cc02896j, 2019.
1067

1068

1069 Penner, J. E., Xu, L. and Wang, M.: Satellite methods underestimate indirect climate forcing by
1070 aerosols., *Proc. Natl. Acad. Sci. U. S. A.*, 108(33), 13404–13408, doi:10.1073/pnas.1018526108,
1071 2011.
1072

1073 Praske, E., Otkjær, R. V., Crouse, J. D., Hethcox, J. C., Stoltz, B. M., Kjaergaard, H. G. and
1074 Wennberg, P. O.: Atmospheric autoxidation is increasingly important in urban and suburban North
1075 America, *Proc. Natl. Acad. Sci.*, 115(1), 64–69, doi:10.1073/pnas.1715540115, 2018.
1076

1077 Quéléver, L. L. J., Kristensen, K., Normann Jensen, L., Rosati, B., Teiwes, R., Daellenbach, K. R.,
1078 Peräkylä, O., Roldin, P., Bossi, R., Pedersen, H. B., Glasius, M., Bilde, M. and Ehn, M.: Effect of
1079 temperature on the formation of highly oxygenated organic molecules (HOMs) from alpha-pinene
1080 ozonolysis, *Atmos. Chem. Phys.*, 19, 7609–7625, doi:10.5194/acp-19-7609-2019, 2019.
1081

1082 Querol, X., Gangoiti, G., Mantilla, E., Alastuey, A., Minguillón, M. C., Amato, F., Reche, C., Viana,
1083 M., Moreno, T., Karanasiou, A., Rivas, I., Pérez, N., Ripoll, A., Brines, M., Ealo, M., Pandolfi, M.,
1084 Lee, H. K., Eun, H. R., Park, Y. H., Escudero, M., Beddows, D., Harrison, R. M., Bertrand, A.,
1085 Marchand, N., Liasota, A., Codina, B., Olid, M., Udina, M., Jiménez-Esteve, B., Jiménez-Esteve, B.
1086 B., Alonso, L., Millán, M. and Ahn, K. H.: Phenomenology of high-ozone episodes in NE Spain,
1087 *Atmos. Chem. Phys.*, 17(4), 2817–2838, doi:10.5194/acp-17-2817-2017, 2017.
1088

1089 Reche, C., Viana, M., Karanasiou, A., Cusack, M., Alastuey, A., Artiñano, B., Revuelta, M. A.,
1090 López-Mahía, P., Blanco-Heras, G., Rodríguez, S., Sánchez de la Campa, A. M., Fernández-
1091 Camacho, R., González-Castanedo, Y., Mantilla, E., Tang, Y. S. and Querol, X.: Urban NH₃ levels
1092 and sources in six major Spanish cities, *Chemosphere*, 119, 769–777,
1093 doi:10.1016/j.chemosphere.2014.07.097, 2015.
1094

1095 Riccobono, F., Schobesberger, S., Scott, C., Dommen, J., Ortega, I., Rondo, L., Almeida, J., Amorim,
1096 A., Bianchi, F., Breitenlechner, M., David, A., Downard, A., Dunne, E., Duplissy, J., Ehrhart, S.,
1097 Flagan, R., Franchin, A., Hansel, A., Junninen, H., Kajos, M., Keskinen, H., Kupc, A., Kürten, A.,
1098 Kvashin, A., Laaksonen, A., Lehtipalo, K., Makhmutov, V., Mathot, S., Nieminen, T., Onnela, A.,
1099 Petäjä, T., Praplan, A., Santos, F., Schallhart, S., Seinfeld, J., Sipilä, M., Van Spracklen, D., Stozhkov,
1100 Y., Stratmann, F., Tomé, A., Tsagkogeorgas, G., Vaattovaara, P., Viisanen, Y., Vrtala, A., Wagner,
1101 P., Weingartner, E., Wex, H., Wimmer, D., Carslaw, K., Curtius, J., Donahue, N., Kirkby, J.,
1102 Kulmala, M., Worsnop, D. and Baltensperger, U.: Oxidation products of biogenic emissions
1103 contribute to nucleation of atmospheric particles., *Science* ~~(80. —)~~, 344(6185), 717–721,
1104 doi:10.1126/science.1243527, 2014.
1105
1106

1107 Rissanen, M. P.: NO₂ Suppression of Autoxidation-Inhibition of Gas-Phase Highly Oxidized Dimer
1108 Product Formation, ACS Earth Sp. Chem., 2(11), 1211–1219,
1109 doi:10.1021/acsearthspacechem.8b00123, 2018.
1110

1111 Rose, C., Zha, Q., Dada, L., Yan, C., Lehtipalo, K., Junninen, H., Mazon, S. B., Jokinen, T., Sarnela,
1112 N., Sipilä, M., Petäjä, T., Kerminen, V.-M., Bianchi, F. and Kulmala, M.: Observations of biogenic
1113 ion-induced cluster formation in the atmosphere, Sci. Adv., 4(4), 5218, doi:10.1126/sciadv.aar5218,
1114 2018.
1115

1116 Schervish, M. and Donahue, N. M.: Peroxy radical chemistry and the volatility basis set, Atmos.
1117 Chem. Phys., 20(2), 1183–1199, doi:10.5194/acp-20-1183-2020, 2020.
1118

1119 Schobesberger, S., Junninen, H., Bianchi, F., Lönn, G., Ehn, M., Lehtipalo, K., Dommen, J., Ehrhart,
1120 S., Ortega, I. K., Franchin, A., Nieminen, T., Riccobono, F., Hutterli, M., Duplissy, J., Almeida, J.,
1121 Amorim, A., Breitenlechner, M., Downard, A. J., Dunne, E. M., Flagan, R. C., Kajos, M., Keskinen,
1122 H., Kirkby, J., Kupc, A., Kürten, A., Kurtén, T., Laaksonen, A., Mathot, S., Onnela, A., Praplan, A.
1123 P., Rondo, L., Santos, F. D., Schallhart, S., Schnitzhofer, R., Sipilä, M., Tomé, A., Tsagkogeorgas,
1124 G., Vehkamäki, H., Wimmer, D., Baltensperger, U., Carslaw, K. S., Curtius, J., Hansel, A., Petäjä,
1125 T., Kulmala, M., Donahue, N. M. and Worsnop, D. R.: Molecular understanding of atmospheric
1126 particle formation from sulphuric acid and large oxidized organic molecules., Proc. Natl. Acad. Sci.
1127 U. S. A., 110(43), 17223–17228, doi:10.1073/pnas.1306973110, 2013.
1128

1129 Simon, M., Heinritzi, M., Herzog, S., Leiminger, M., Bianchi, F., Praplan, A., Dommen, J., Curtius,
1130 J. and KürtenKürten, A.: Detection of dimethylamine in the low pptv range using nitrate chemical
1131 ionization atmospheric pressure interface time-of-flight (CI-API-TOF) mass spectrometry, Atmos.
1132 Meas. Tech., 9(5), 2135–2145, doi:10.5194/amt-9-2135-2016, 2016.
1133

1134 Sipilä, M., Sarnela, N., Jokinen, T., Henschel, H., Junninen, H., Kontkanen, J., Richters, S.,
1135 Kangasluoma, J., Franchin, A., Peräkylä, O., Rissanen, M. P., Ehn, M., Vehkamäki, H.,
1136 KürtenKürten, T., Berndt, T., Petäjä, T., Worsnop, D., Ceburnis, D., Kerminen, V. M., Kulmala, M.
1137 and O'Dowd, C.: Molecular-scale evidence of aerosol particle formation via sequential addition of
1138 HIO₃, Nature, 537(7621), 532–534, doi:10.1038/nature19314, 2016.
1139

1140 Stolzenburg, D., Fischer, L., Vogel, A. L., Heinritzi, M., Schervish, M., Simon, M., Wagner, A. C.,
1141 Dada, L., Ahonen, L. R., Amorim, A., Baccarini, A., Bauer, P. S., Baumgartner, B., Bergen, A.,
1142 Bianchi, F., Breitenlechner, M., Brilke, S., Buenrostro Mazon, S., Chen, D., Dias, A., Draper, D. C.,
1143 Duplissy, J., El Haddad, I., Finkenzeller, H., Frege, C., Fuchs, C., Garmash, O., Gordon, H., He, X.,
1144 Helm, J., Hofbauer, V., Hoyle, C. R., Kim, C., Kirkby, J., Kontkanen, J., Kürten, A., Lampilahti, J.,
1145 Lawler, M., Lehtipalo, K., Leiminger, M., Mai, H., Mathot, S., Mentler, B., Molteni, U., Nie, W.,
1146 Nieminen, T., Nowak, J. B., Ojdanic, A., Onnela, A., Passananti, M., Petäjä, T., Quéléver, L. L. J.,
1147 Rissanen, M. P., Sarnela, N., Schallhart, S., Tauber, C., Tomé, A., Wagner, R., Wang, M., Weitz, L.,
1148 Wimmer, D., Xiao, M., Yan, C., Ye, P., Zha, Q., Baltensperger, U., Curtius, J., Dommen, J., Flagan,
1149 R. C., Kulmala, M., Smith, J. N., Worsnop, D. R., Hansel, A., Donahue, N. M. and Winkler, P. M.:
1150 Rapid growth of organic aerosol nanoparticles over a wide tropospheric temperature range,
1151 [P. Natl. Acad. Sci. USA, 115, 9122–9127, 2018.](https://doi.org/10.1073/pnas.1807604115)
1152 ~~[Proc. Natl. Acad. Sci.,](https://doi.org/10.1073/pnas.1807604115)~~
1153 ~~[201807604 \[online\] Available from: <http://www.pnas.org/lookup/doi/10.1073/pnas.1807604115>,](https://doi.org/10.1073/pnas.1807604115)~~
1154 ~~[2018.](https://doi.org/10.1073/pnas.1807604115)~~
1155

1156 Tröstl, J., Chuang, W. K., Gordon, H., Heinritzi, M., Yan, C., Molteni, U., Ahlm, L., Frege, C.,
1157 Bianchi, F., Wagner, R., Simon, M., Lehtipalo, K., Williamson, C., Craven, J. S., Duplissy, J.,
1158 Adamov, A., Almeida, J., Bernhammer, A. K., Breitenlechner, M., Brilke, S., Dias, A., Ehrhart, S.,

1159 Flagan, R. C., Franchin, A., Fuchs, C., Guida, R., Gysel, M., Hansel, A., Hoyle, C. R., Jokinen, T.,
1160 Junninen, H., Kangasluoma, J., Keskinen, H., Kim, J., Krapf, M., Kürten, A., Laaksonen, A., Lawler,
1161 M., Leiminger, M., Mathot, S., Möhler, O., Nieminen, T., Onnela, A., Petäjä, T., Piel, F. M.,
1162 Miettinen, P., Rissanen, M. P., Rondo, L., Sarnela, N., Schobesberger, S., Sengupta, K., Sipilä, M.,
1163 Smith, J. N., Steiner, G., Tomè, A., Virtanen, A., Wagner, A. C., Weingartner, E., Wimmer, D.,
1164 Winkler, P. M., Ye, P., Carslaw, K. S., Curtius, J., Dommen, J., Kirkby, J., Kulmala, M., Riipinen, I.,
1165 Worsnop, D. R., Donahue, N. M. and Baltensperger, U.: The role of low-volatility organic compounds
1166 in initial particle growth in the atmosphere, *Nature*, 533(7604), 527–531, doi:10.1038/nature18271,
1167 2016.

1168

1169 Van Damme, M., Clarisse, L., Whitburn, S., Hadji-Lazaro, J., Hurtmans, D., Clerbaux, C. and
1170 Coheur, P. F.: Industrial and agricultural ammonia point sources exposed, *Nature*, 564(7734), 99–
1171 103, doi:10.1038/s41586-018-0747-1, 2018.

1172

1173 Wang, S., Wu, R., Berndt, T., Ehn, M. and Wang, L.: Formation of Highly Oxidized Radicals and
1174 Multifunctional Products from the Atmospheric Oxidation of Alkylbenzenes, *Environ. Sci. Technol.*,
1175 51(15), 8442–8449, doi:10.1021/acs.est.7b02374, 2017.

1176

1177 ~~Yan, C.: The role of H₂SO₄-NH₃ anion clusters in ion-induced aerosol nucleation mechanisms in the~~
1178 ~~boreal forest, *Atmos. Chem. Phys.*, (April), 1–20, doi:10.1029/2001JD001100, 2018.~~

1179

1180 Yan, C., Nie, W., Äijälä, M., Rissanen, M. P., Canagaratna, M. R., Massoli, P., Junninen, H., Jokinen,
1181 T., Sarnela, N., Häme, S. A. K., Schobesberger, S., Canonaco, F., Yao, L., Prévôt, A. S. H., Petäjä,
1182 T., Kulmala, M., Sipilä, M., Worsnop, D. R. and Ehn, M.: Source characterization of highly oxidized
1183 multifunctional compounds in a boreal forest environment using positive matrix factorization, *Atmos.*
1184 *Chem. Phys.*, 16(19), 12715–12731, doi:10.5194/acp-16-12715-2016, 2016.

1185

1186 Yan, C., Dada, L., Rose, C., Jokinen, T., Nie, W., Schobesberger, S., Junninen, H., Lehtipalo, K.,
1187 Sarnela, N., Makkonen, U., Garmash, O., Wang, Y., Zha, Q., Paasonen, P., Bianchi, F., Sipilä, M.,
1188 Ehn, M., Petäjä, T., Kerminen, V.-M., Worsnop, D. R., and Kulmala, M.: The role of H₂SO₄-NH₃
1189 anion clusters in ion-induced aerosol nucleation mechanisms in the boreal forest, *Atmos. Chem.*
1190 *Phys.*, 18, 13231–13243, <https://doi.org/10.5194/acp-18-13231-2018>, 2018.

1191

1192 Yan, C., Nie, W., Vogel, A. L., Dada, L., Lehtipalo, K., Stolzenburg, D., Wagner, R., Rissanen, M.
1193 P., Xiao, M., Ahonen, L., Fischer, L., Rose, C., Bianchi, F., Gordon, H., Simon, M., Heinritzi, M.,
1194 Garmash, O., Roldin, P., Dias, A., Ye, P., Hofbauer, V., Amorim, A., Bauer, P. S., Bergen, A.,
1195 Bernhammer, A.-K., Breitenlechner, M., Brilke, S., Buchholz, A., Mazon, S. B., Canagaratna, M. R.,
1196 Chen, X., Ding, A., Dommen, J., Draper, D. C., Duplissy, J., Frege, C., Heyn, C., Guida, R., Hakala,
1197 J., Heikkinen, L., Hoyle, C. R., Jokinen, T., Kangasluoma, J., Kirkby, J., Kontkanen, J., Kürten, A.,
1198 Lawler, M. J., Mai, H., Mathot, S., Mauldin, R. L., Molteni, U., Nichman, L., Nieminen, T., Nowak,
1199 J., Ojdanic, A., Onnela, A., Pajunoja, A., Petäjä, T., Piel, F., Quéléver, L. L. J., Sarnela, N., Schallhart,
1200 S., Sengupta, K., Sipilä, M., Tomé, A., Tröstl, J., Väisänen, O., Wagner, A. C., Ylisirniö, A., Zha, Q.,
1201 Baltensperger, U., Carslaw, K. S., Curtius, J., Flagan, R. C., Hansel, A., Riipinen, I., Smith, J. N.,
1202 Virtanen, A., Winkler, P. M., Donahue, N. M., Kerminen, V.-M., Kulmala, M., Ehn, M. and Worsnop,
1203 D. R.: Size-dependent influence of NO_x on the growth rates of organic aerosol particles, *Sci. Adv.*,
1204 6(22), eaay4945, doi:10.1126/sciadv.aay4945, 2020.

1205

1206 Yao, L., Garmash, O., Bianchi, F., Zheng, J., Yan, C., Kontkanen, J., Junninen, H., Mazon, S. B.,
1207 Ehn, M., Paasonen, P., Sipilä, M., Wang, M., Wang, X., Xiao, S., Chen, H., Lu, Y., Zhang, B., Wang,
1208 D., Fu, Q., Geng, F., Li, L., Wang, H., Qiao, L., Yang, X., Chen, J., Kerminen, V. M., Petäjä, T.,
1209 Worsnop, D. R., Kulmala, M. and Wang, L.: Atmospheric new particle formation from sulphuric acid
1210 and amines in a Chinese megacity, *Science*—(80.—), 361(6399), 278–281,

1211 doi:10.1126/science.aao4839, 2018.

1212

1213 Yli-Juuti, T., Pajunoja, A., Tikkanen, O. P., Buchholz, A., Faiola, C., Väisänen, O., Hao, L., Kari, E.,
1214 Peräkylä, O., Garmash, O., Shiraiwa, M., Ehn, M., Lehtinen, K. and Virtanen, A.: Factors controlling
1215 the evaporation of secondary organic aerosol from α -pinene ozonolysis, *Geophys. Res. Lett.*, 44(5),
1216 2562–2570, doi:10.1002/2016GL072364, 2017.

1217

1218 Yu, H., Zhou, L., Dai, L., Shen, W., Dai, W., Zheng, J., Ma, Y. and Chen, M.: Nucleation and growth
1219 of sub-3 nm particles in the polluted urban atmosphere of a megacity in China, *Atmos. Chem. Phys.*,
1220 16(4), 2641–2657, doi:10.5194/acp-16-2641-2016, 2016.

1221

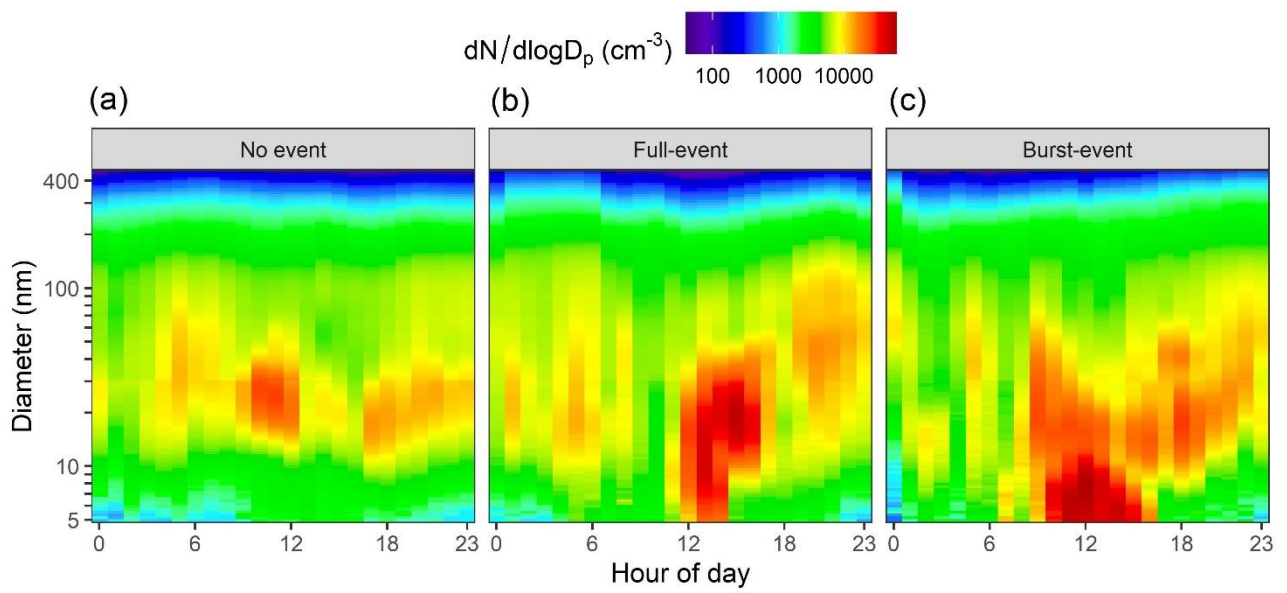
1222 Zhang, R., Khalizov, A., Wang, L., Hu, M. and Xu, W.: Nucleation and growth of nanoparticles in
1223 the atmosphere, *Chem. Rev.*, 112(3), 1957–2011, doi:10.1021/cr2001756, 2012.

1224

1225 Zhao, J., Eisele, F. L., Titcombe, M., Kuang, C. and McMurry, P. H.: Chemical ionization mass
1226 spectrometric measurements of atmospheric neutral clusters using the cluster-CIMS, *J. Geophys.*
1227 *Res.*, 115(D8), 1–19, doi:10.1029/2009jd012606, 2010.

1228

1229

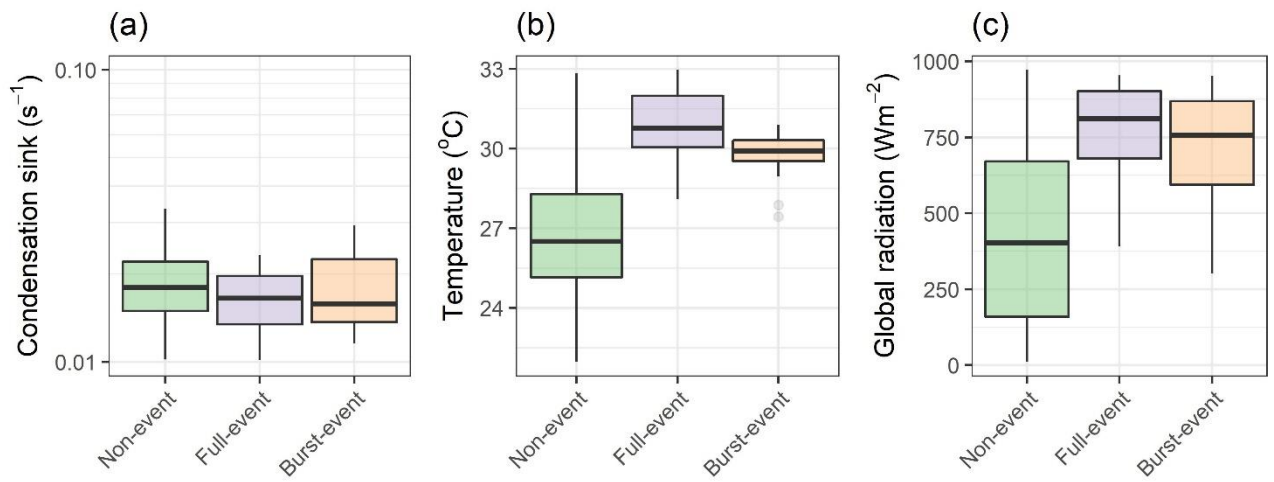
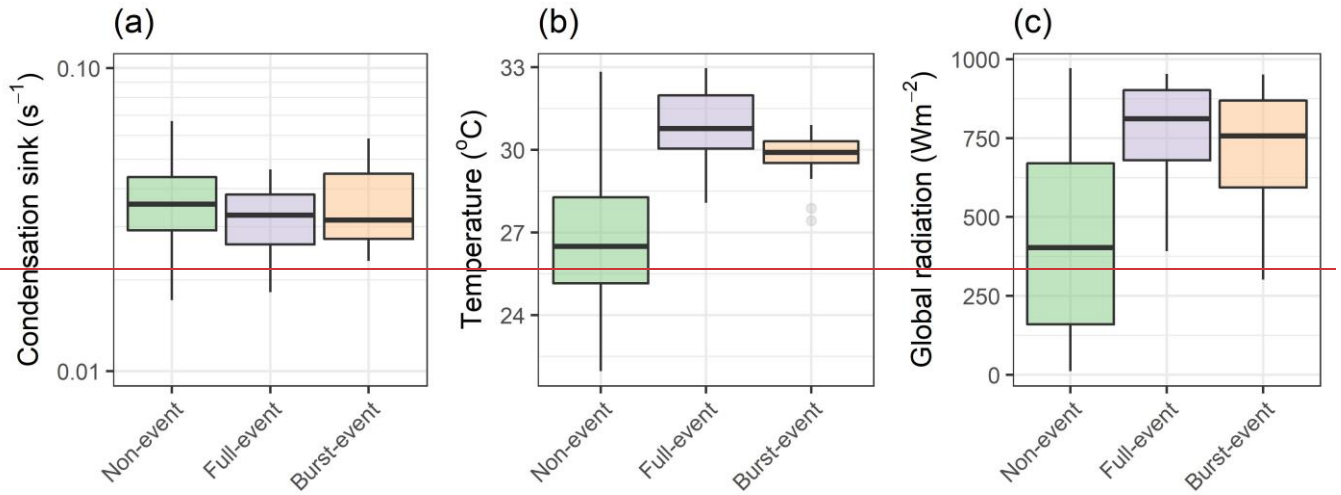


1231

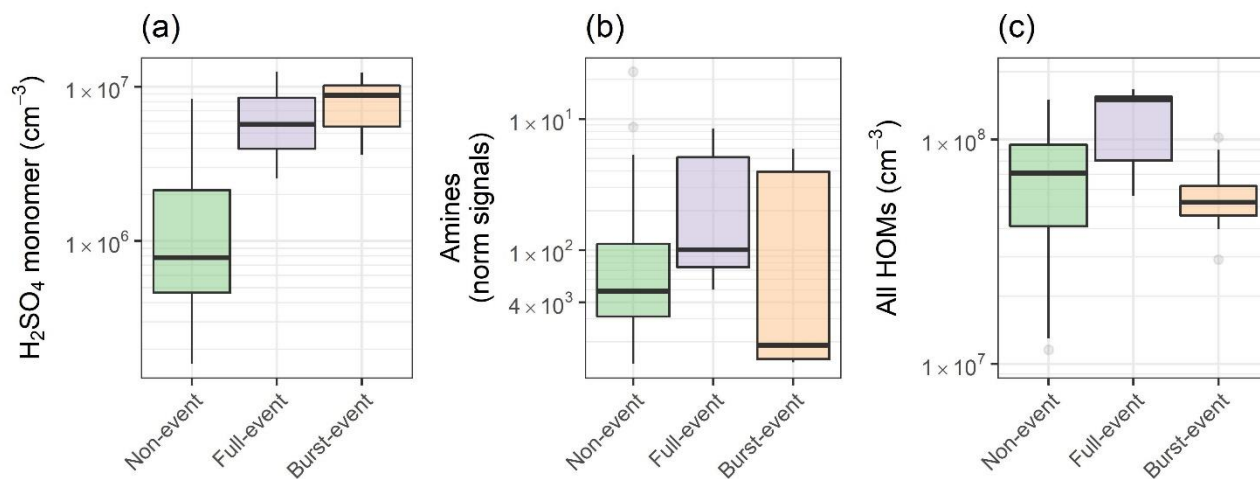
1232 **Figure 1:** Average SMPS contour plots for (a) non-event days, (b) full-event days and (c) burst-event
1233 days.

1234

1235



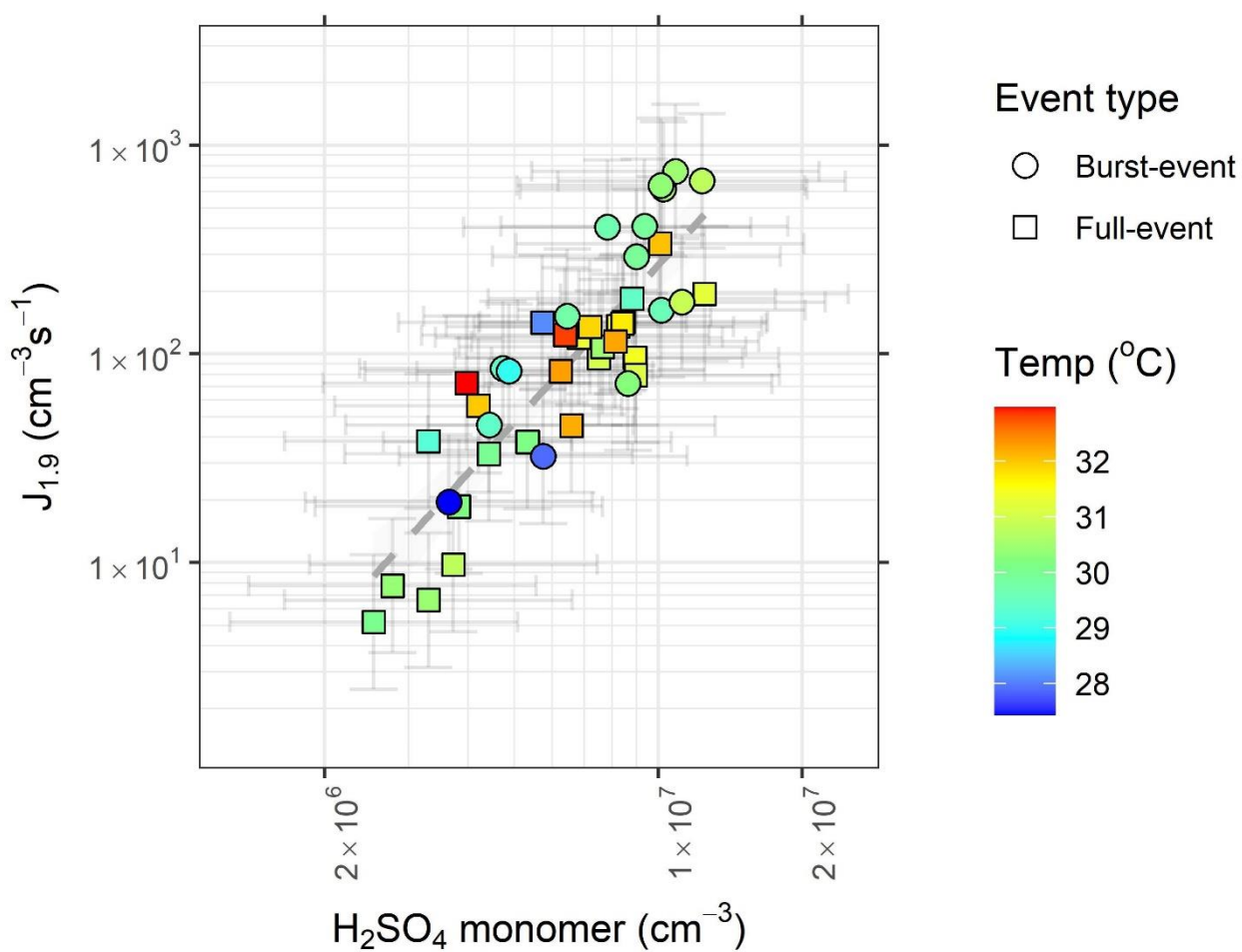
1239 **Figure 2:** Box plots for days of non-event, full-event and burst-event, showing (a) condensation sink,
 1240 (b) temperature, and (c) global radiation from hourly data. “Full-event” and “burst-event” include
 1241 data across the entire day.



1244

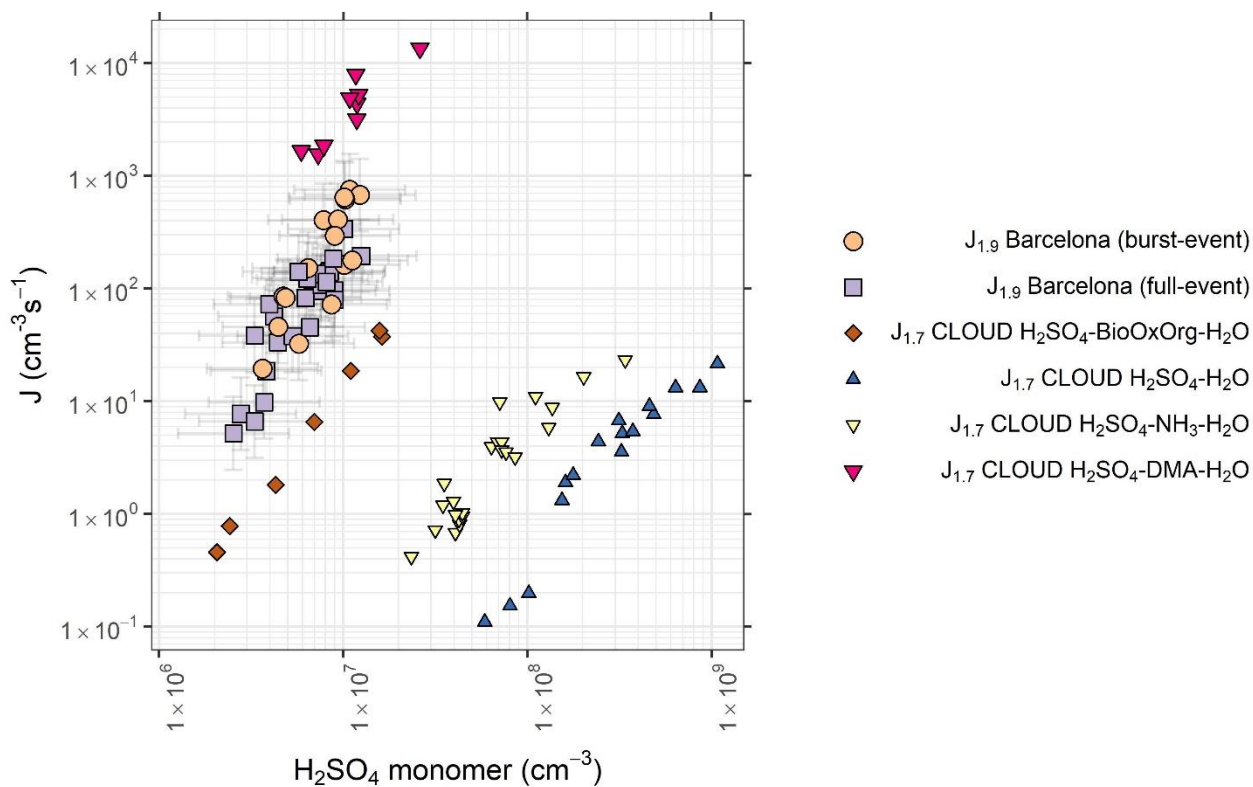
1245 **Figure 3:** Box plots for days of non-event, full-event and burst-event, showing (a) sulphuric acid, (b)
 1246 C_2 and C_4 amines, as clustered with the nitrate dimer and trimer, and (c) summed HOM concentration
 1247 from C_{5+} from hourly data. Units for ammonia + amines are normalised counts, as no calibration was
 1248 performed. Event days include data across the full event day.

1249



1251

1252 **Figure 4:** Formation rate ($J_{1.9}$) plotted against sulphuric acid monomer concentration, coloured by
 1253 condensation sink. Circles represent burst-events, squares represent full events. Data is for hourly
 1254 averages across NPF periods, typically within the hours 08:00 – 16:00. Slope of the line = $4.9 \cdot 10^{-5} \text{ s}^{-1}$.
 1255 Error bars represent systematic uncertainties on $[\text{H}_2\text{SO}_4]$ and $J_{1.9}$

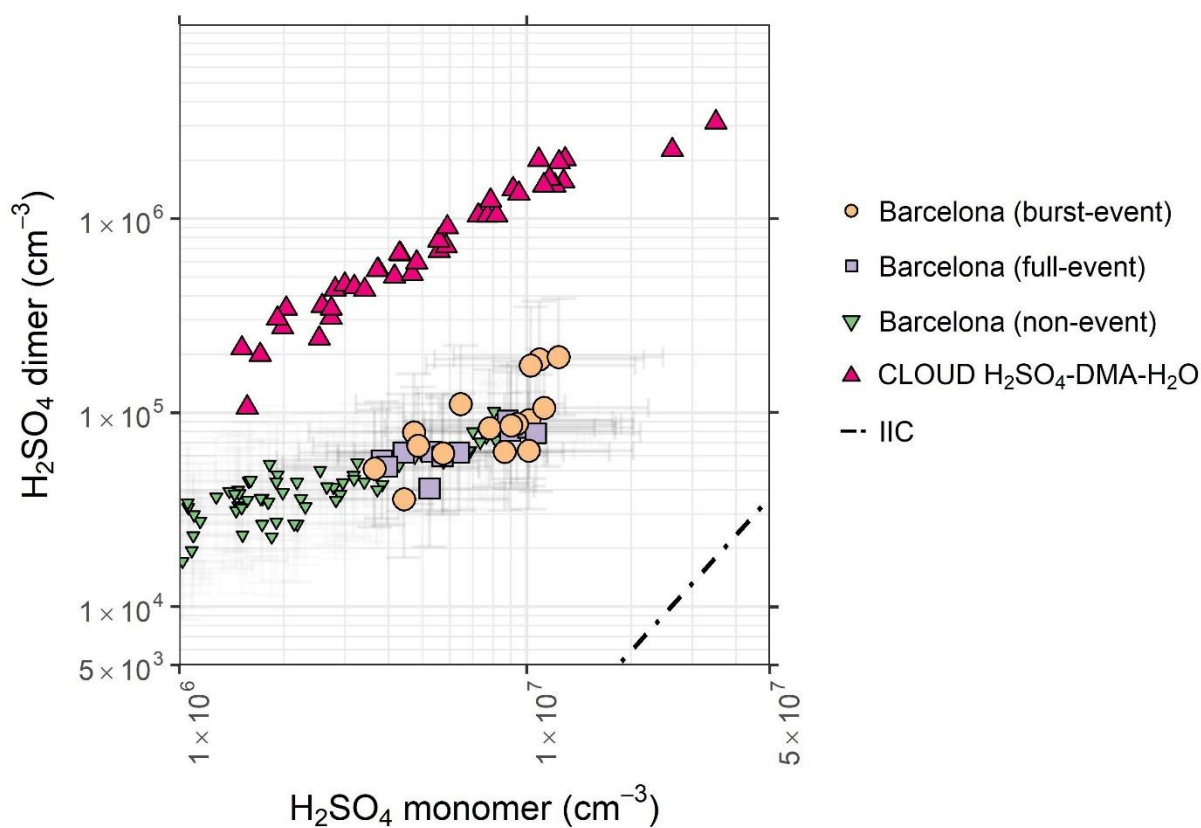


1256

1257 **Figure 5:** Formation rate plotted against sulphuric acid monomer concentration for data collected
 1258 from Barcelona. Tan circles represent burst-events, purple squares represent full events. as well as
 1259 that for the H₂SO₄-H₂O (blue inverted triangles), H₂SO₄-NH₃-H₂O (yellow inverted triangles),
 1260 H₂SO₄-DMA-H₂O (pink triangles), and H₂SO₄-BioOxOrg-H₂O (brown diamonds) systems from the
 1261 CLOUD chamber (Kürten et al., 2018 Kirkby et al., 2011; Riccobono et al., 2014). CLOUD
 1262 chamber experiments were performed at 278 K and 38 – 39 % RH. Data is for hourly averages
 1263 across NPF periods, typically within the hours 08:00 – 16:00. Error bars represent systematic
 1264 uncertainties on [H₂SO₄] and J_{1,9}.

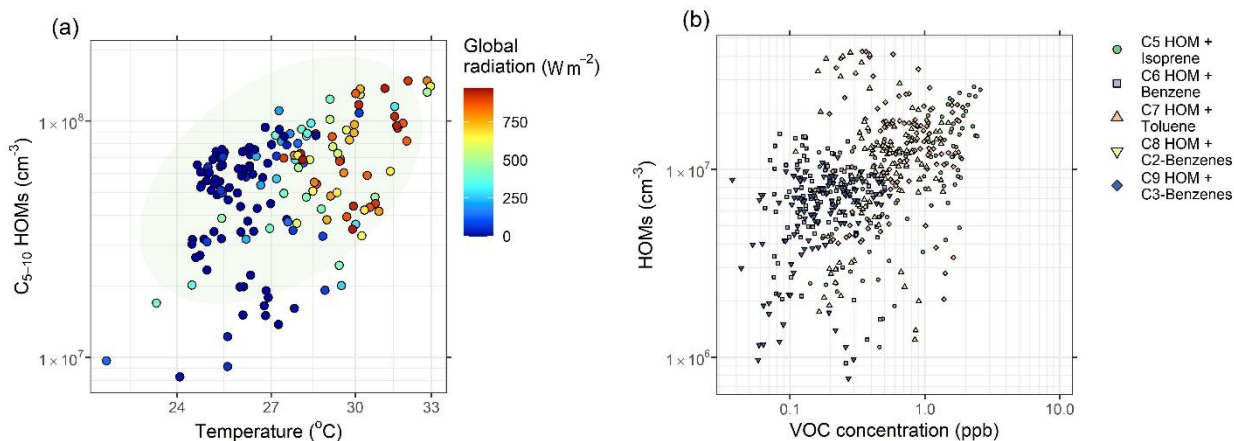
1265

1266



1267
 1268 **Figure 6:** Sulphuric acid dimer concentration plotted against monomer concentration, showing burst-
 1269 event periods (tan circles), full event periods (purple squares), non-event periods (green inverted
 1270 triangles), and the ratio of sulphuric acid dimer:monomer in the CLOUD chamber for the H_2SO_4 -
 1271 H_2O -DMA system (pink triangles) (Almeida et al., 2013). Dashed line represents the dimer
 1272 concentration produced by ion induced clustering in the chemical ionization unit (Zhao et al., 2010).
 1273 CLOUD chamber experiments were performed at 278 K and 38 – 39 % RH. Data is for hourly
 1274 averages across NPF periods, typically within the hours 08:00 – 16:00. Error bars represent systematic
 1275 uncertainties on $[\text{H}_2\text{SO}_4]$ and $[(\text{H}_2\text{SO}_4)_2]$.

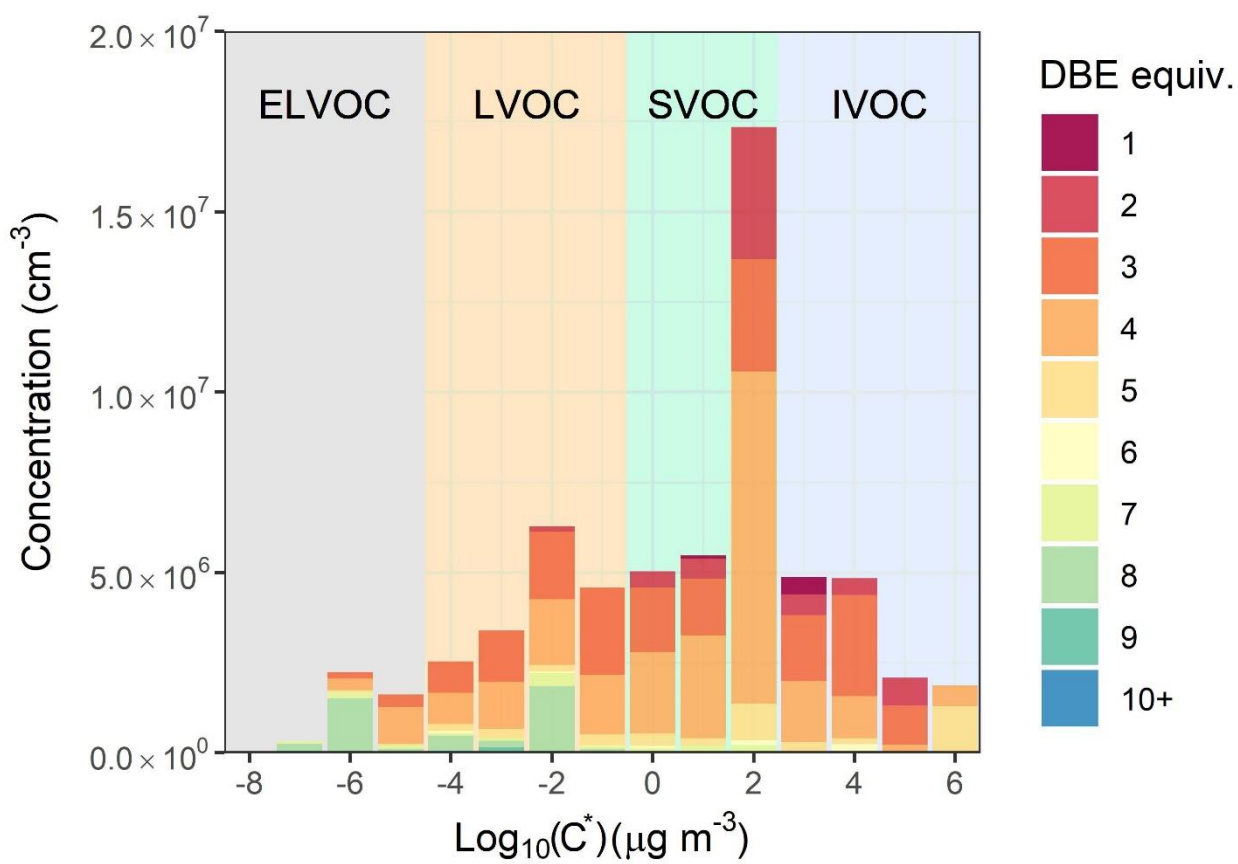
1276



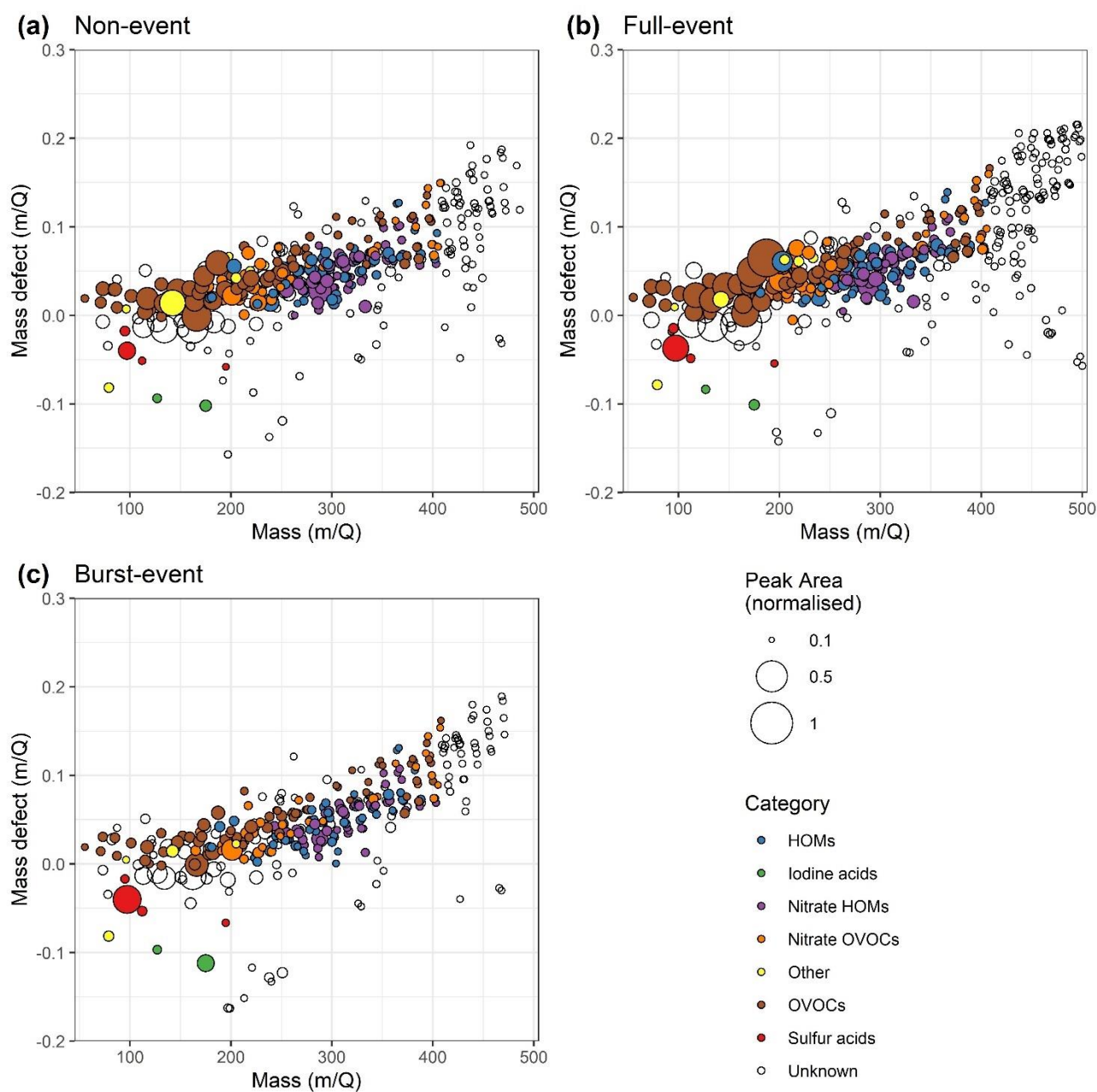
1278

1279 **Figure 7:** Influencing factors on HOM concentration, showing (a) C₅₋₁₀ HOM concentration plotted
 1280 against temperature, coloured by global radiation. Ellipsis shows 95% confidence on a multivariate
 1281 t-distribution. (b) HOM concentration by carbon number plotted against parent VOC mixing ratio.
 1282 These are segregated by carbon number/VOC, i.e. C₇ HOMs plotted against toluene, under the
 1283 assumption that toluene oxidation is the main producer of C₇ HOMs. Time for both plots is of hourly
 1284 time resolution.

1285



1288 **Figure 8:** Concentrations of all oxygenated organic molecules and HOMs binned to integer $\text{Log}_{10}(C^*)$
 1289 values, coloured by DBE.



1290

1291 **Figure 9:** Mass defect plots for (a) non-event, (b) full-event, and (c) burst-event periods, data taken
 1292 from 10:00 – 15:00 on the days 11/07/2018, 16/07/2018 and 15/07/2018 respectively. Size
 1293 corresponds to mass spectral peak area. Ions are coloured according to identified chemical
 1294 composition. *Blue* points correspond to HOMs containing all organic species with ≥ 5 carbon atoms
 1295 and ≥ 6 oxygen atoms, and an O:C ratio of >0.6 . *Purple* points correspond to the same but for species
 1296 containing 1-2 nitrogen atoms. Species not meeting this HOM criteria were classed generally as
 1297 OVOCs which are coloured *brown*, with the nitrogen containing OVOCs coloured *orange*. Sulphur
 1298 acids (*red*) include ions HSO_4^- , CH_3SO_3^- and SO_5^- , as well as the sulphuric acid dimer. Iodine acids
 1299 (*green*) contains both IO_3^- and I^- (the latter presumably deprotonated hydrogen iodide). Unidentified
 1300 points are left uncoloured.

1301

1302

Supplementary Information

1303

1304

Molecular Insights into New Particle Formation in Barcelona, Spain

1305

1306

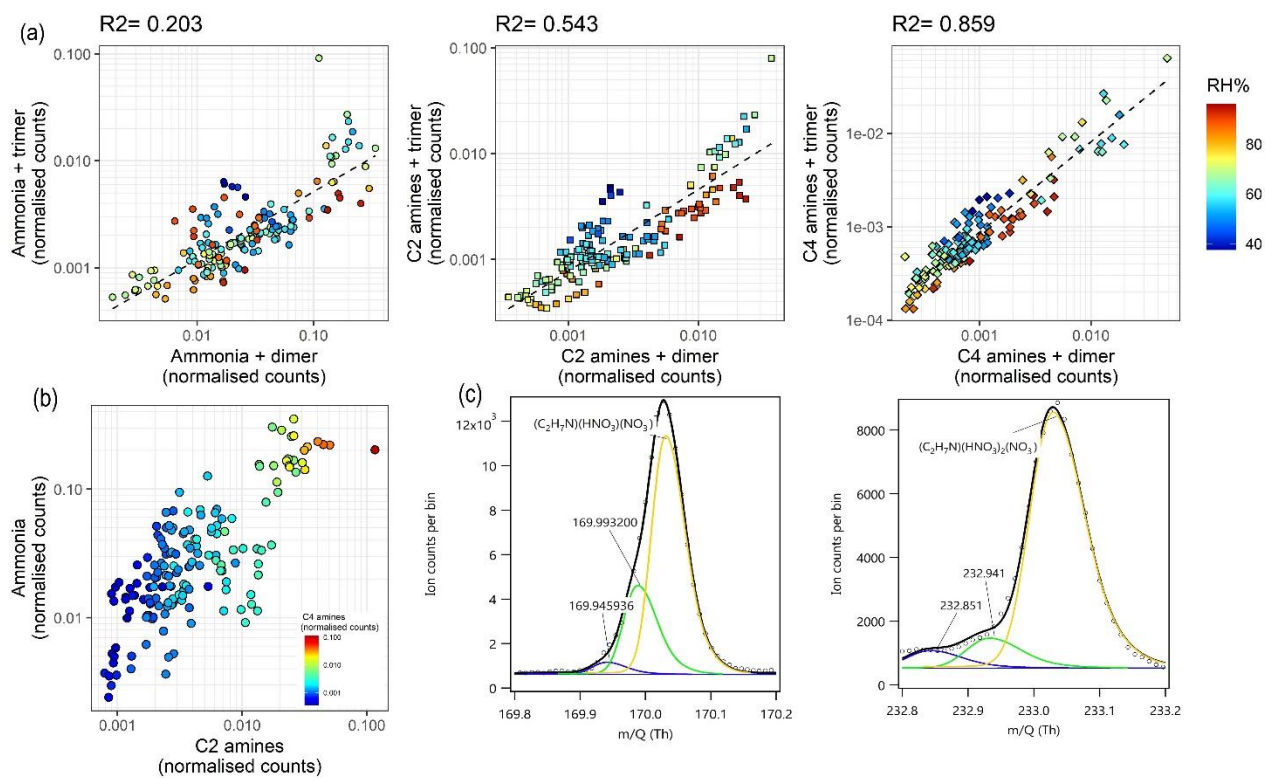
1307

**James Brean, David C.S. Beddows, Zongbo Shi, Brice Temime-Roussel,
Nicolas Marchand, Xavier Querol, Andrés Alastuey, María Cruz
Minguillón, and Roy M. Harrison**

1308

1309

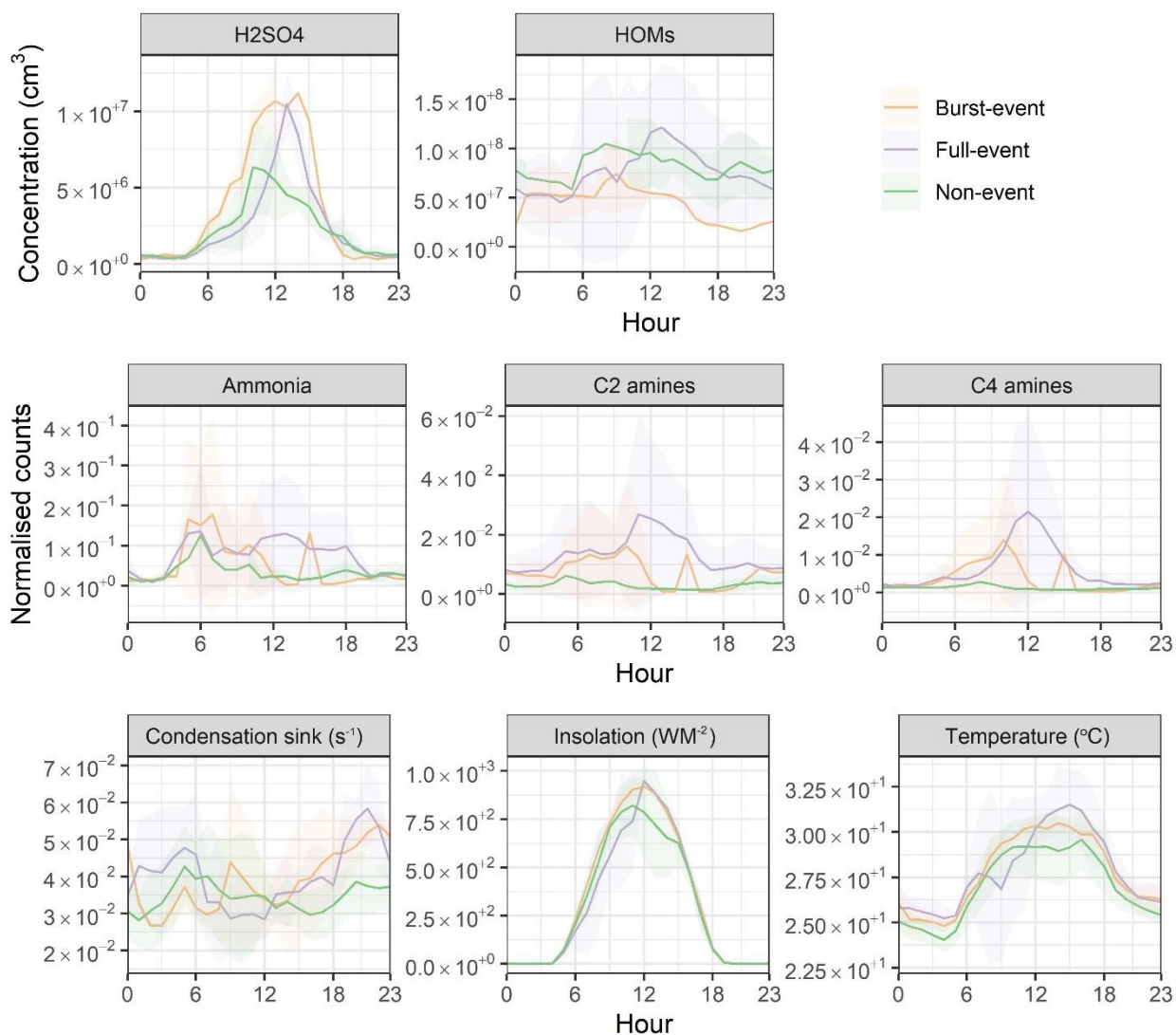
1310

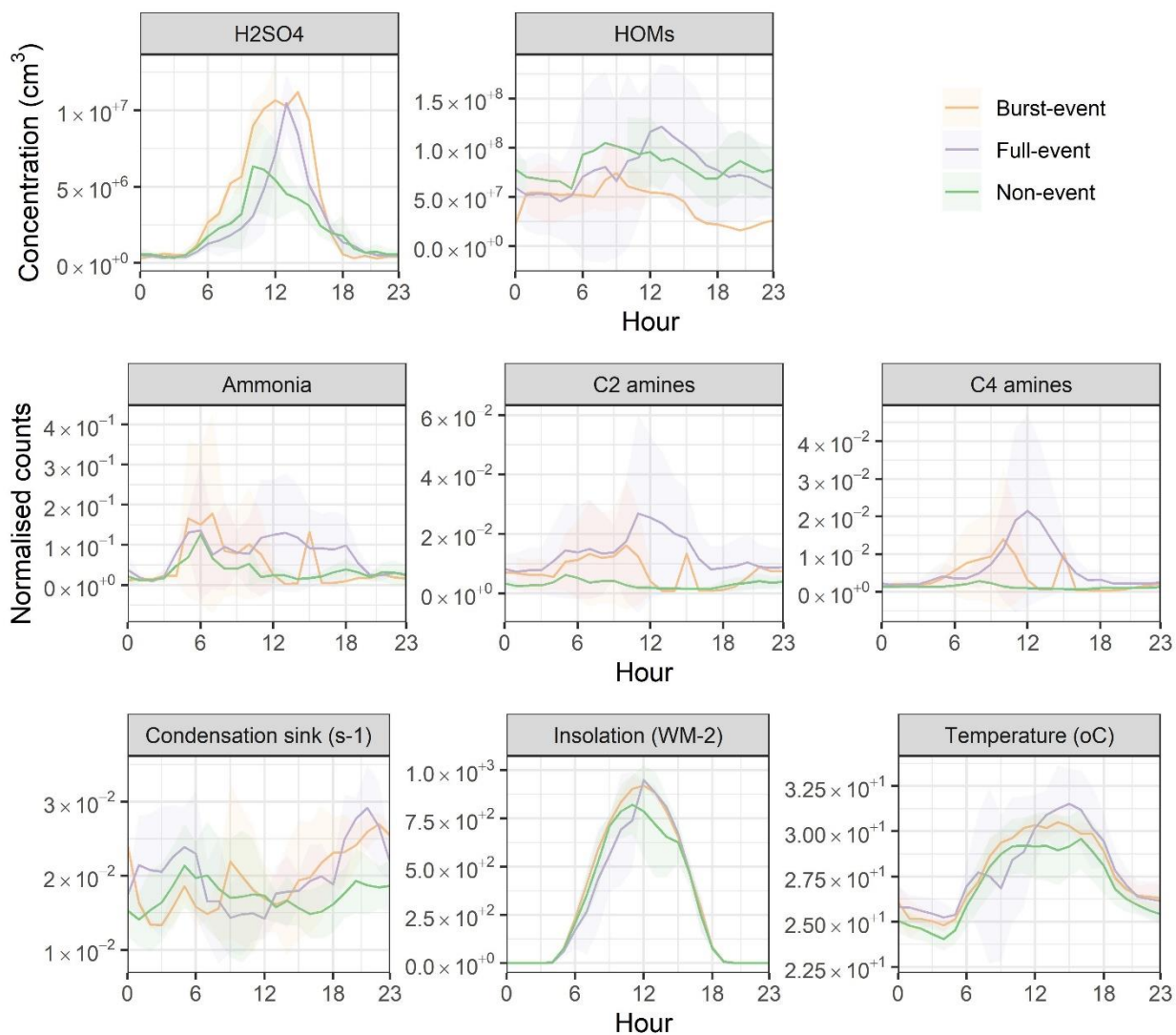


1311

1312 **Figure S1:** Ammonia and amine measurements via CI-API-ToF, showing (a) ammonia, C₂
 1313 and C₄ amines as measured clustered with the nitrate dimer and trimer. Colour scale shows an
 1314 RH dependence. (b) Ammonia plotted against C₂ amines, coloured by C₄ amine concentration,
 1315 and (c) peak fits for the C₂ amine ion as clustered with the nitrate dimer and trimer.

1316

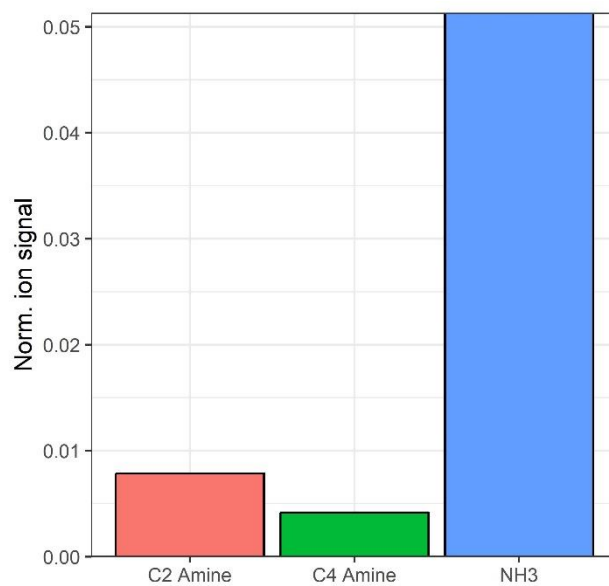




1318

1319
1320
1321

Figure S2: Diurnal profiles of (from top left through bottom right), H₂SO₄, HOMs, NH₃, C₂ amines, C₄ amines, condensation sink, insolation and temperature. Shaded regions show 1 standard deviation on the mean.

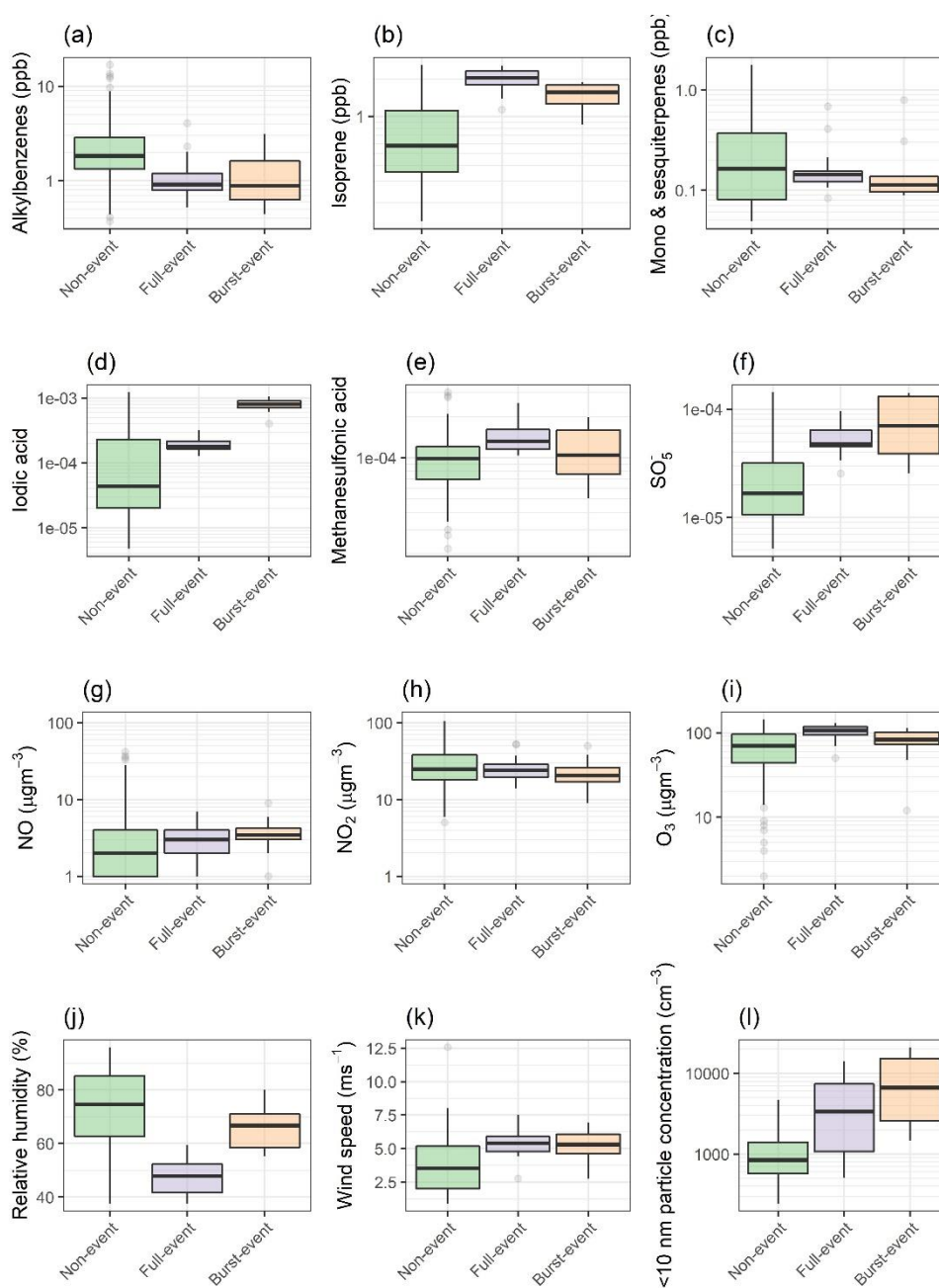


1322

1323

1324

Figure S3: Mean ammonia and amine signals across the campaign as measured by CI-APi-ToF. Units of normalised ion counts.



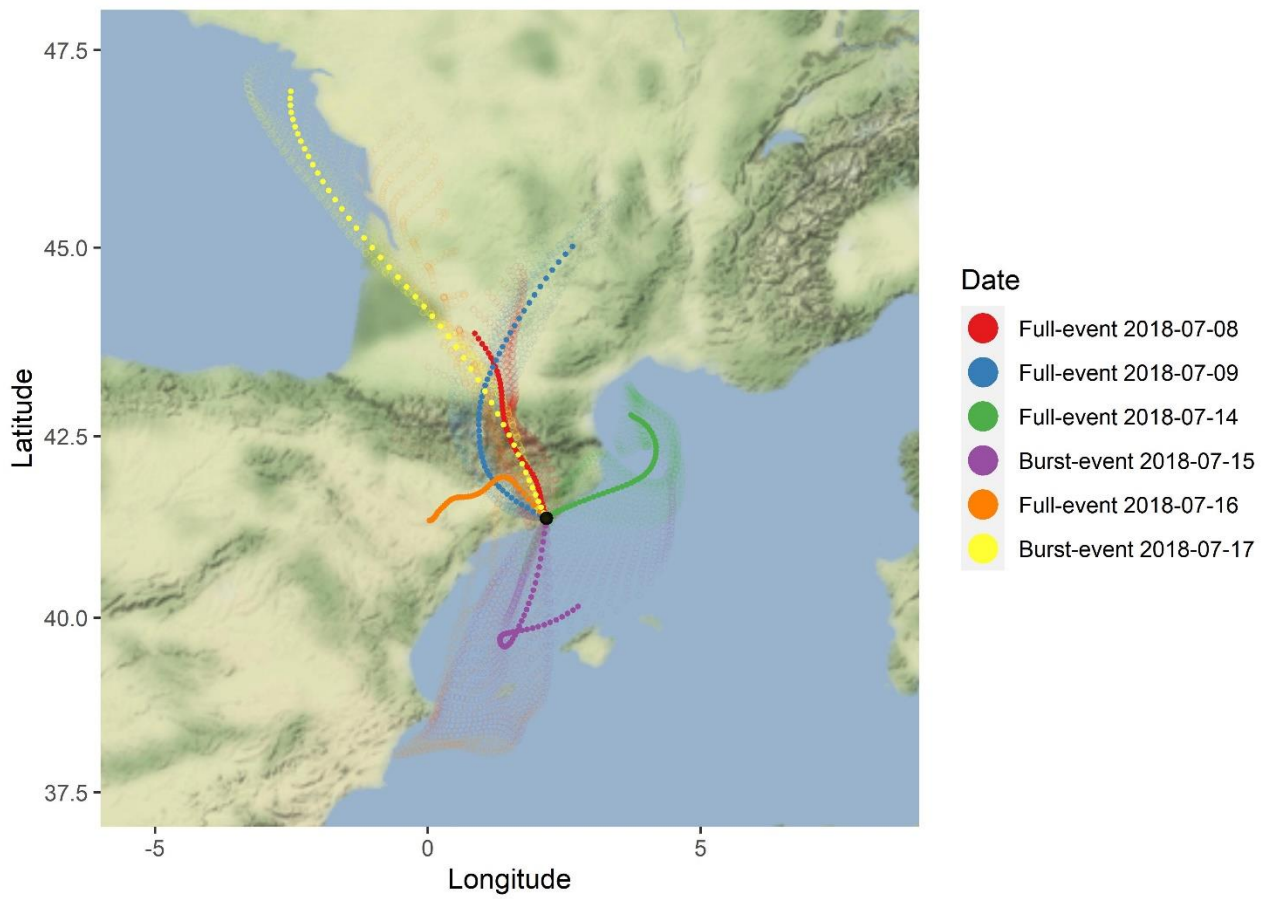
1325

1326

1327

1328

Figure S4: Box plots as figures 2 & 3 for (a-c) VOCs as measured by PTR-ToF-MS, (d-f) other ions as measured by CI-APi-ToF (units of norm. counts) (g-i) trace gases, and (j-l) meteorological and <10 nm particle count parameters.



1329

1330

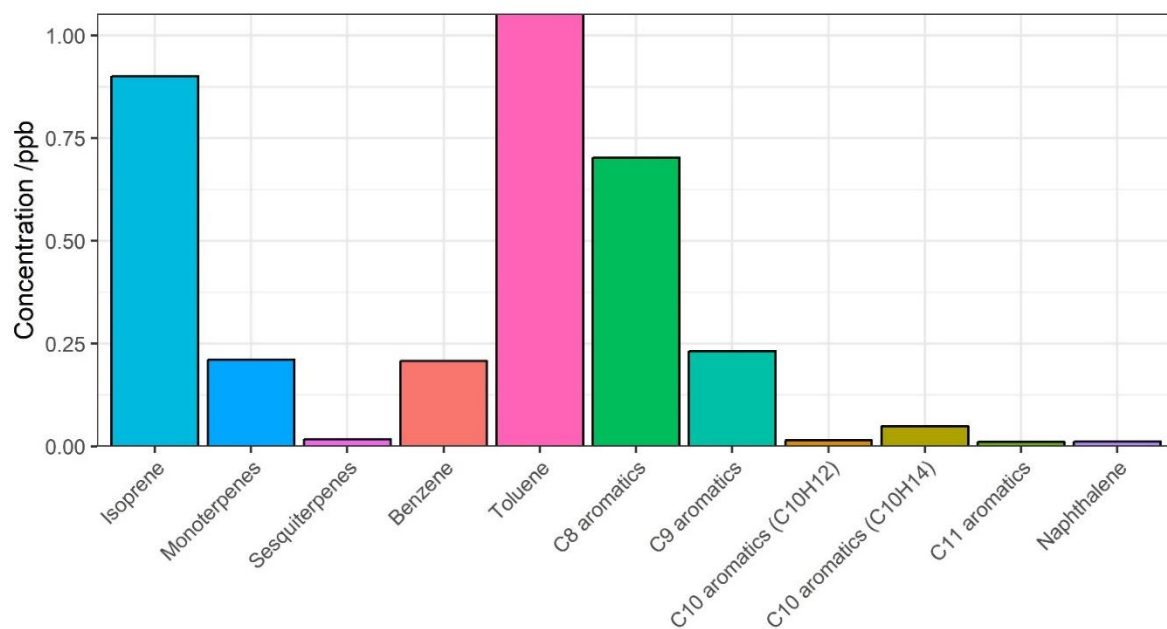
1331

1332

1333

1334

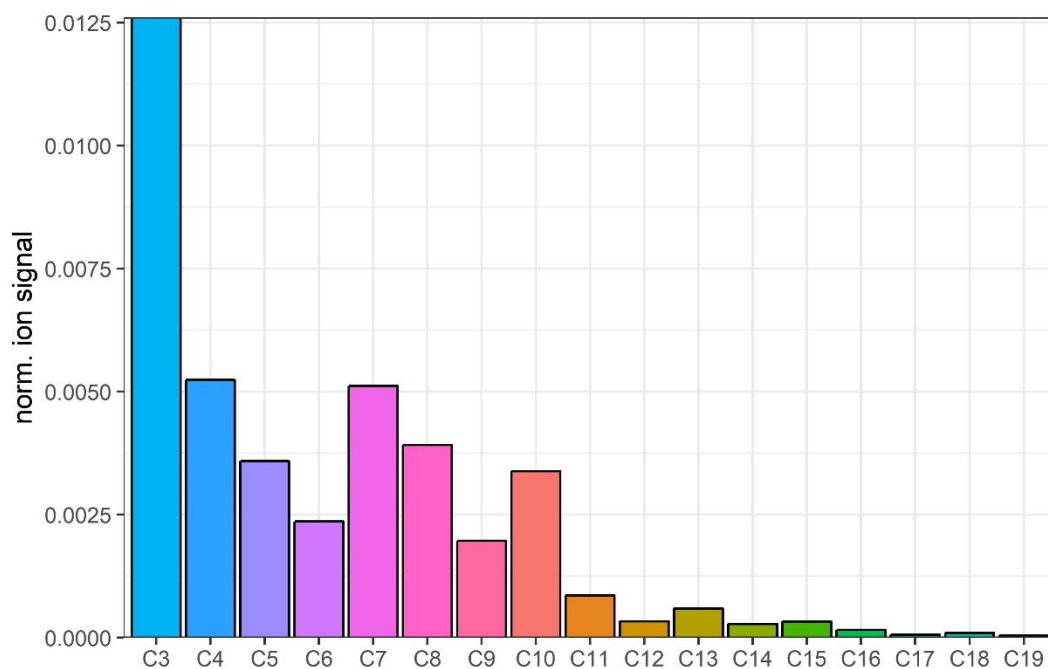
Figure S5: HYSPLIT 96 hour back trajectories per nucleation event. Dark dashed lines show mean trajectory per event, light dashed lines show hourly trajectories from which mean is calculated.



1335

1336 **Figure S6:** Mean selected VOC concentrations across the campaign as measured by PTR-
 1337 ToF-MS.

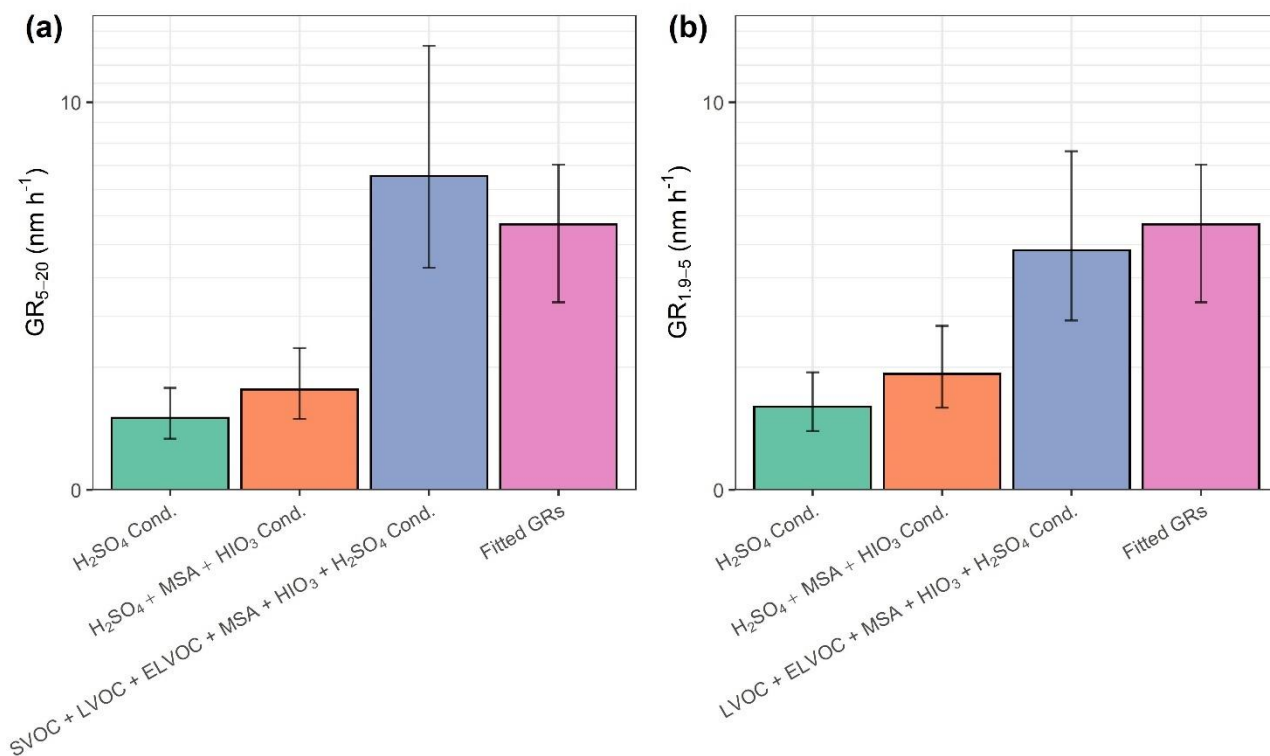
1338



1339

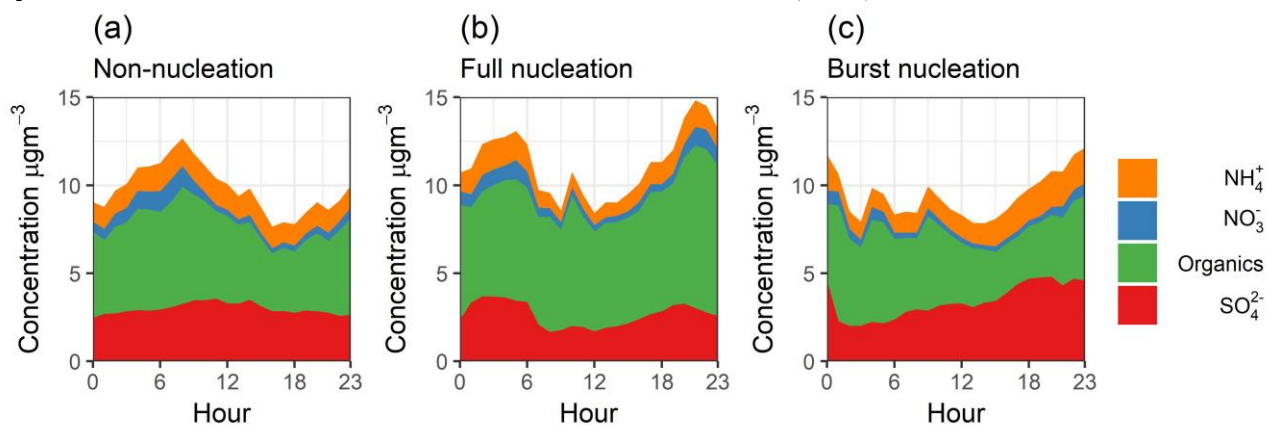
1340 **Figure S7:** Mean ion signals per carbon number across the campaign as measured by CI-
 1341 APi-ToF. Units of normalised ion counts.

1342



1344

1345 **Figure S8:** Condensational growth rates between-in the ranges (a) 5 - 20 nm and (b) 1.9 – 5 nm,
 1346 calculated from H_2SO_4 condensation, H_2SO_4 , MSA, and HIO_3 condensation, and SVOC, LVOC,
 1347 ELVOC, H_2SO_4 , MSA and HIO_3 in (a), and LVOC, ELVOC, H_2SO_4 , MSA and HIO_3 in (b). Also
 1348 presented are growth rates from particle count data. Error bars represent uncertainties on the
 1349 concentration of species measured by CI-APi-ToF, and the uncertainties from GR calculations.
 1350 Systematic uncertainties from the methods of Nieminen et al. (2010) are not included.

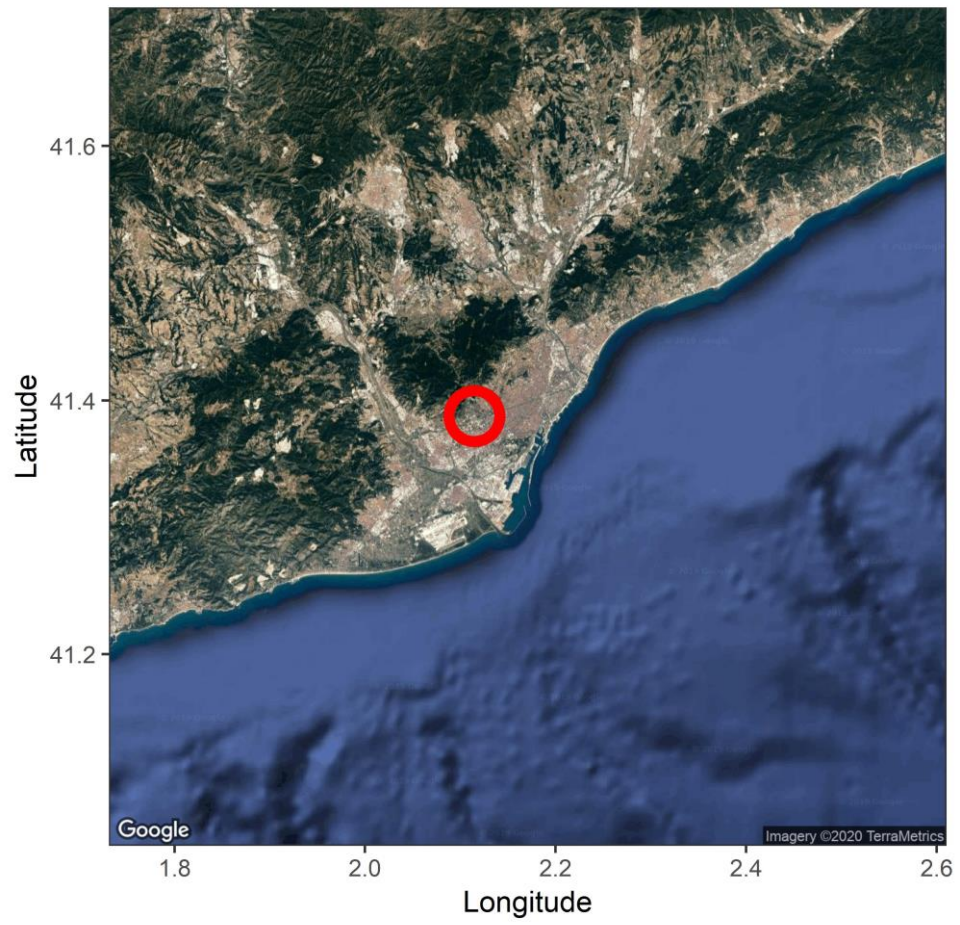


1351

1352 **Figure S9:** Average diurnals of particle composition as measured by ACSM on (a) non-
 1353 nucleation, (b) full-nucleation and (c) burst-nucleation days.

1354

1355



1356

1357

1358

Figure S10: Location of sampling site.

Table 1: Ions identified by CI-APi-ToF

Ion	m/Q
Cl ⁻	34.97
NO ₂ ⁻	45.99
C ₃ H ₃ O ⁻	55.02
(NO ₃) ⁻	61.99
C ₃ H ₃ O ₂ ⁻	71.01
C ₃ H ₅ O ₂ ⁻	73.03
Br ⁻	78.92
H ₂ O(NO ₃) ⁻	80.00
C ₄ H ₅ O ₂ ⁻	85.03
C ₃ H ₃ O ₃ ⁻	87.01
CH ₃ SO ₃ ⁻	94.98
CFH ₃ (NO ₃) ⁻	96.01
HSO ₄ ⁻	96.96
HCl(NO ₃) ⁻	97.97
H ₄ O ₂ (NO ₃) ⁻	98.01
C ₄ H ₅ O ₃ ⁻	101.02
C ₃ H ₃ O ₄ ⁻	103.00
SO ₅ ⁻	111.95
C ₄ H ₃ O ₄ ⁻	115.00
C ₄ H ₅ O ₄ ⁻	117.02
C ₃ H ₄ O(NO ₃) ⁻	118.01
C ₃ H ₃ O ₅ ⁻	119.00
HNO ₃ NO ₃ ⁻	124.98
I ⁻	126.91
C ₄ H ₃ O ₅ ⁻	131.00
C ₅ H ₇ O ₄ ⁻	131.03
C ₄ H ₅ O ₅ ⁻	133.01
NH ₃ (HNO ₃)(NO ₃) ⁻	142.01
C ₅ H ₅ O ₅ ⁻	145.01
C ₅ H ₇ O ₅ ⁻	147.03
C ₃ H ₆ O ₃ (NO ₃) ⁻	152.02
C ₆ H ₇ O ₅ ⁻	159.03
C ₄ H ₆ O ₃ (NO ₃) ⁻	164.02
C ₃ H ₅ NO ₃ (NO ₃) ⁻	165.02
C ₃ H ₄ O ₄ (NO ₃) ⁻	166.00
C ₆ H ₅ NO(NO ₃) ⁻	169.03
C ₂ H ₇ N(HNO ₃)(NO ₃) ⁻	170.04
C ₇ H ₇ O ₅ ⁻	171.03
C ₇ H ₉ O ₅ ⁻	173.05
IO ₃ ⁻	174.89
C ₄ H ₅ NO ₃ (NO ₃) ⁻	177.02
C ₄ H ₄ O ₄ (NO ₃) ⁻	178.00
C ₅ H ₇ O ₇ ⁻	179.02

$C_4H_6O_4(NO_3)^-$	180.01
$C_5H_9O_7^-$	181.04
$C_4H_8O_4(NO_3)^-$	182.03
$C_8H_{11}O_5^-$	187.06
$(HNO_3)_2(NO_3)^-$	187.98
$C_7H_9O_6^-$	189.04
$C_5H_7NO_3(NO_3)^-$	191.03
$C_4H_6N_2O_3(NO_3)^-$	192.03
$C_4H_5NO_4(NO_3)^-$	193.01
$C_5H_8O_4(NO_3)^-$	194.03
$H_2SO_4HSO_4^-$	194.93
$C_5H_7O_8^-$	195.01
$C_3H_6N_2O_4(NO_3)^-$	196.02
$C_4H_8O_5(NO_3)^-$	198.03
$C_4H_{11}N(HNO_3)(NO_3)^-$	198.07
$C_7H_7NO_2(NO_3)^-$	199.04
$C_6H_5NO_3(NO_3)^-$	201.02
$C_8H_{11}O_6^-$	203.06
$C_6H_6O_4(NO_3)^-$	204.01
$NH_3(HNO_3)_2(NO_3)^-$	205.01
$C_6H_8O_4(NO_3)^-$	206.03
$C_5H_7NO_4(NO_3)^-$	207.03
$C_4H_6N_2O_4(NO_3)^-$	208.02
$C_5H_8O_5(NO_3)^-$	210.03
$C_4H_7NO_5(NO_3)^-$	211.02
$C_8H_6O_3(NO_3)^-$	212.02
$C_3H_5NO_6(NO_3)^-$	213.00
$C_{10}H_{13}O_5^-$	213.08
$C_4H_8O_6(NO_3)^-$	214.02
$C_7H_7NO_3(NO_3)^-$	215.03
$C_7H_6O_4(NO_3)^-$	216.01
$C_7H_9NO_3(NO_3)^-$	217.05
$C_7H_8O_4(NO_3)^-$	218.03
$C_7H_{10}O_4(NO_3)^-$	220.05
$C_6H_9NO_4(NO_3)^-$	221.04
$C_5H_8N_2O_4(NO_3)^-$	222.04
$C_{10}H_7O_6^-$	223.02
$C_5H_8O_6(NO_3)^-$	226.02
$C_4H_7NO_6(NO_3)^-$	227.02
$C_4H_6O_7(NO_3)^-$	228.00
$C_8H_9NO_3(NO_3)^-$	229.05
$C_7H_7NO_4(NO_3)^-$	231.03
$C_2H_7N(HNO_3)_2(NO_3)^-$	233.04
$C_7H_{10}O_5(NO_3)^-$	236.04
$C_7H_{12}O_5(NO_3)^-$	238.06
$C_{10}H_7O_7^-$	239.02

$C_4H_6N_2O_6(NO_3)^-$	240.01
$C_5H_8O_7(NO_3)^-$	242.02
$C_5H_{11}NO_6(NO_3)^-$	243.05
$C_5H_{10}O_7(NO_3)^-$	244.03
$C_9H_{12}O_4(NO_3)^-$	246.06
$C_7H_7NO_5(NO_3)^-$	247.02
$C_8H_{10}O_5(NO_3)^-$	248.04
$C_7H_9NO_5(NO_3)^-$	249.04
$C_8H_{12}O_5(NO_3)^-$	250.06
$C_7H_{11}NO_5(NO_3)^-$	251.05
$C_7H_{10}O_6(NO_3)^-$	252.04
$C_7H_{12}O_6(NO_3)^-$	254.05
$C_6H_{11}NO_6(NO_3)^-$	255.05
$C_6H_{10}O_7(NO_3)^-$	256.03
$C_5H_8O_8(NO_3)^-$	258.01
$C_8H_7NO_5(NO_3)^-$	259.02
$C_9H_{10}O_5(NO_3)^-$	260.04
$C_4H_{11}N(HNO_3)_2(NO_3)^-$	261.07
$C_9H_{12}O_5(NO_3)^-$	262.06
$C_7H_7NO_6(NO_3)^-$	263.02
$C_8H_{11}NO_5(NO_3)^-$	263.05
$C_8H_{10}O_6(NO_3)^-$	264.04
$C_9H_{14}O_5(NO_3)^-$	264.07
$C_7H_9NO_6(NO_3)^-$	265.03
$C_7H_8O_7(NO_3)^-$	266.01
$C_8H_{12}O_6(NO_3)^-$	266.05
$C_7H_{11}NO_6(NO_3)^-$	267.05
$C_8H_{15}NO_5(NO_3)^-$	267.08
$C_7H_{10}O_7(NO_3)^-$	268.03
$C_6H_{11}NO_7(NO_3)^-$	271.04
$C_6H_{10}O_8(NO_3)^-$	272.03
$C_5H_9NO_8(NO_3)^-$	273.02
$C_5H_8O_9(NO_3)^-$	274.01
$C_{10}H_{12}O_5(NO_3)^-$	274.06
$C_{10}H_{14}O_5(NO_3)^-$	276.07
$C_9H_{13}NO_5(NO_3)^-$	277.07
$C_9H_{12}O_6(NO_3)^-$	278.05
$C_{10}H_{16}O_5(NO_3)^-$	278.09
$C_8H_{11}NO_6(NO_3)^-$	279.05
$C_9H_{14}O_6(NO_3)^-$	280.07
$C_7H_9NO_7(NO_3)^-$	281.03
$C_8H_{12}O_7(NO_3)^-$	282.05
$C_7H_{11}NO_7(NO_3)^-$	283.04
$C_8H_{14}O_7(NO_3)^-$	284.06
$C_{10}H_9NO_5(NO_3)^-$	285.04
$C_5H_8N_2O_8(NO_3)^-$	286.02

$C_5H_7NO_9(NO_3)^-$	287.00
$C_7H_{15}NO_7(NO_3)^-$	287.07
$C_5H_{10}N_2O_8(NO_3)^-$	288.03
$C_5H_9NO_9(NO_3)^-$	289.02
$C_{10}H_{12}O_6(NO_3)^-$	290.05
$C_{10}H_{15}NO_5(NO_3)^-$	291.08
$C_{10}H_{14}O_6(NO_3)^-$	292.07
$C_9H_{13}NO_6(NO_3)^-$	293.06
$C_{10}H_{16}O_6(NO_3)^-$	294.08
$C_8H_{11}NO_7(NO_3)^-$	295.04
$C_9H_{14}O_7(NO_3)^-$	296.06
$C_8H_{13}NO_7(NO_3)^-$	297.06
$C_8H_{12}O_8(NO_3)^-$	298.04
$C_7H_{10}O_9(NO_3)^-$	300.02
$C_{10}H_9NO_6(NO_3)^-$	301.03
$C_7H_{12}O_9(NO_3)^-$	302.04
$C_{10}H_{11}NO_6(NO_3)^-$	303.05
$C_6H_{10}O_{10}(NO_3)^-$	304.02
$C_{12}H_{18}O_5(NO_3)^-$	304.10
$C_9H_9NO_7(NO_3)^-$	305.03
$C_9H_8O_8(NO_3)^-$	306.01
$C_{11}H_{16}O_6(NO_3)^-$	306.08
$C_{10}H_{15}NO_6(NO_3)^-$	307.08
$C_{10}H_{14}O_7(NO_3)^-$	308.06
$C_9H_{13}NO_7(NO_3)^-$	309.06
$C_{10}H_{16}O_7(NO_3)^-$	310.08
$C_9H_{15}NO_7(NO_3)^-$	311.07
$C_9H_{14}O_8(NO_3)^-$	312.06
$C_8H_{13}NO_8(NO_3)^-$	313.05
$C_8H_{12}O_9(NO_3)^-$	314.04
$C_7H_{11}NO_9(NO_3)^-$	315.03
$C_{10}H_{10}N_2O_6(NO_3)^-$	316.04
$C_{10}H_9NO_7(NO_3)^-$	317.03
$C_{12}H_{16}O_6(NO_3)^-$	318.08
$C_{10}H_{11}NO_7(NO_3)^-$	319.04
$C_{10}H_{10}O_8(NO_3)^-$	320.03
$C_{12}H_{18}O_6(NO_3)^-$	320.10
$C_{10}H_{13}NO_7(NO_3)^-$	321.06
$C_{11}H_{16}O_7(NO_3)^-$	322.08
$C_{10}H_{15}NO_7(NO_3)^-$	323.07
$C_{10}H_{14}O_8(NO_3)^-$	324.06
$C_{10}H_{16}O_8(NO_3)^-$	326.07
$C_9H_{15}NO_8(NO_3)^-$	327.07
$C_9H_{14}O_9(NO_3)^-$	328.05
$C_8H_{13}NO_9(NO_3)^-$	329.05
$C_9H_{16}O_9(NO_3)^-$	330.07

$C_{11}H_{11}NO_7(NO_3)^-$	331.04
$C_{10}H_9NO_8(NO_3)^-$	333.02
$C_{12}H_{16}O_7(NO_3)^-$	334.08
$C_{12}H_{18}O_7(NO_3)^-$	336.09
$C_{10}H_{13}NO_8(NO_3)^-$	337.05
$C_{11}H_{16}O_8(NO_3)^-$	338.07
$C_{10}H_{15}NO_8(NO_3)^-$	339.07
$C_{10}H_{14}O_9(NO_3)^-$	340.05
$C_{13}H_{13}NO_6(NO_3)^-$	341.06
$C_{10}H_{16}O_9(NO_3)^-$	342.07
$C_9H_{15}NO_9(NO_3)^-$	343.06
$C_9H_{14}O_{10}(NO_3)^-$	344.05
$C_{12}H_{13}NO_7(NO_3)^-$	345.06
$C_{13}H_{16}O_7(NO_3)^-$	346.08
$C_{13}H_{18}O_7(NO_3)^-$	348.09
$C_{12}H_{17}NO_7(NO_3)^-$	349.09
$C_{13}H_{20}O_7(NO_3)^-$	350.11
$C_{11}H_{15}NO_8(NO_3)^-$	351.07
$C_{11}H_{17}NO_8(NO_3)^-$	353.08
$C_{10}H_{15}NO_9(NO_3)^-$	355.06
$C_{11}H_{18}O_9(NO_3)^-$	356.08
$C_{10}H_{17}NO_9(NO_3)^-$	357.08
$C_{13}H_{14}O_8(NO_3)^-$	360.06
$C_{12}H_{13}NO_8(NO_3)^-$	361.05
$C_{13}H_{19}NO_7(NO_3)^-$	363.10
$C_{13}H_{18}O_8(NO_3)^-$	364.09
$C_{12}H_{17}NO_8(NO_3)^-$	365.08
$C_{13}H_{20}O_8(NO_3)^-$	366.10
$C_{12}H_{19}NO_8(NO_3)^-$	367.10
$C_{12}H_{18}O_9(NO_3)^-$	368.08
$C_{11}H_{17}NO_9(NO_3)^-$	369.08
$C_{11}H_{16}O_{10}(NO_3)^-$	370.06
$C_{10}H_{15}NO_{10}(NO_3)^-$	371.06
$C_{14}H_{14}O_8(NO_3)^-$	372.06
$C_{13}H_{13}NO_8(NO_3)^-$	373.05
$C_{14}H_{16}O_8(NO_3)^-$	374.07
$C_{14}H_{20}O_8(NO_3)^-$	378.10
$C_{13}H_{19}NO_8(NO_3)^-$	379.10
$C_{14}H_{22}O_8(NO_3)^-$	380.12
$C_{13}H_{21}NO_8(NO_3)^-$	381.12
$C_{13}H_{20}O_9(NO_3)^-$	382.10
$C_{16}H_{19}NO_6(NO_3)^-$	383.11
$C_{16}H_{18}O_7(NO_3)^-$	384.09
$C_{15}H_{17}NO_7(NO_3)^-$	385.09
$C_{15}H_{16}O_8(NO_3)^-$	386.07
$C_{10}H_{15}NO_{11}(NO_3)^-$	387.05

$C_{11}H_{18}O_{11}(NO_3)^-$	388.07
$C_{18}H_{21}N(NO_3)O_5^-$	393.13
$C_{15}H_{24}(NO_3)O_8^-$	394.14
$C_{18}H_{23}N(NO_3)O_5^-$	395.15
$C_{18}H_{22}(NO_3)O_6^-$	396.13
$C_{17}H_{21}N(NO_3)O_6^-$	397.13
$C_{17}H_{20}(NO_3)O_7^-$	398.11
$C_{16}H_{19}N(NO_3)O_7^-$	399.10
$C_{16}H_{18}(NO_3)O_8^-$	400.09
$C_{15}H_{17}N(NO_3)O_8^-$	401.08
$C_{12}H_{20}(NO_3)O_{11}^-$	402.09
$C_{10}H_{15}N(NO_3)O_{12}^-$	403.05
$C_{15}H_{18}(NO_3)O_9^-$	404.08
$C_{18}H_{17}N(NO_3)O_6^-$	405.09
$C_{19}H_{23}N(NO_3)O_5^-$	407.15
$C_{19}H_{22}(NO_3)O_6^-$	408.13

1361

1362

1363